VI. "ATOMIC" APPLICATIONS

In the following section of notes, we will discuss some important astrophysical applications of the processes discussed in §I-V. In all examples, the emphasis will be on the *atomic processes* needed to explain the observed spectra of a certain region or object, rather than on a comprehensive discussion of the region or object itself. The list is, of course, not exhaustive, and interested students should turn to the texts referenced at the beginning of the course for more complete discussions!

1. H⁻ in the Solar Photosphere

The simplest two-electron atomic system is the hydrogen negative ion, H^-. Clearly, H^- differs from He in reduced mass – and, more importantly – in nuclear charge. The smaller nuclear charge in H^- means that the effect of electron-repulsion will be relatively much larger than in helium. In fact, the effect is *so* large that there is only one (singly-excited) bound state of the system.

The ionization potential of H^- is only 0.75 eV (which corresponds to a photon of wavelength 1.64 μm); this is, of course, also the electron affinity of the neutral hydrogen atom. The astrophysical implications are:

(i) $kT \sim 0.75$ eV when T$\sim$9000 K, which is comparable to or greater than the surface temperature of most stars. Thus, in typical stars like the Sun (T_{eff} = 5800 K, H^- can survive in significant abundance. Because most stars consist predominantly of hydrogen; H, e^-, and H^- co-exist in relative amounts dictated by the temperature in the star's atmosphere.

(ii) All cosmically abundant neutral atoms and positive ions have ionization potentials (IPs) $\gtrsim 4.3$ eV, corresponding to photon energies with $\lambda \lesssim 2900$ Å; i.e., they can only absorb radiation at ultraviolet wavelengths continuously. Only H^-, of all abundant atomic species, is capable of absorbing continuously in the visible and infrared, namely $\lambda \lesssim 16420$ Å, due to the process of *photodetachment*
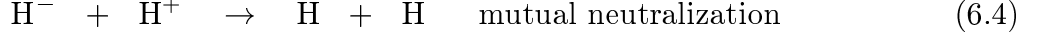
$$H^- \;+\; h\nu \;\;\rightarrow\;\; H \;+\; e^- \;. \tag{6.1}$$
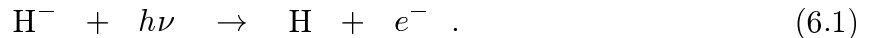
Thus, H^- is a dominant source of opacity in the atmospheres of many stars. Discussions of the cross section for absorption by H^- go back to Chandrasekhar (1944, *Ap. J.* **100**, 176), and include Doughty *et al.* (1966, *MNRAS* **132**, 255) and Macek (1967, *Proc. Phys. Soc.* **92**, 365). The most recent calculations by Wishart (1979, *MNRAS* **187**, 59) are reproduced in Table 6.1.

As in the case of photoionization and recombination, the process of photodetachment has an inverse process called *radiative attachment*

$$H \;+\; e^- \;\;\rightarrow\;\; H^- \;+\; h\nu \;. \tag{6.2}$$
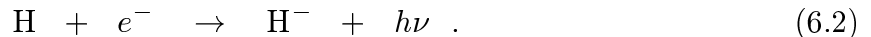
For H^-, the rates of photodetachment in a black-body radiation field of temperature T, and of radiative attachment of thermal electrons at the same T, are given in Table 6.2. Note, however, that various other microscopic process affect H^-, e.g.

$$H^- \;+\; H \;\;\rightarrow\;\; H_2 \;+\; e^- \qquad \text{associative detachment} \tag{6.3}$$

$$\text{H}^- \quad + \quad \text{H}^+ \quad \rightarrow \quad \text{H} \quad + \quad \text{H} \qquad \text{mutual neutralization} \tag{6.4}$$

In the Sun's photosphere, e.g. at $\tau_V \sim 0.3$ where T$\sim$5800 K, $n(\text{H}) \sim 9 \times 10^{16}$ cm^{-3}, $n(e^-) \sim 7 \times 10^{13}$ cm^{-3}, balancing the rates of radiative attachment and photodetachment

$$n(\text{H}^-)\, 2.6 \times 10^6 \quad \sim \quad n(\text{H})n(e^-)\, 2.8 \times 10^{-15} \quad [\text{s}^{-1}], \tag{6.5}$$

implies that $n(\text{H}^-) \sim 6.8 \times 10^9$ cm^{-3}. This estimate is not correct, however, because H$^-$ is removed faster by H via reactions (6.3)!

Table 6.1 – Bound-free photo-detachment cross sections of H$^-$ in
units of 10^{-18} cm^2 as a function of incident photon λ in Å

λ	$\sigma(\lambda)$	λ	$\sigma(\lambda)$	λ	$\sigma(\lambda)$
16300	0.1989	11500	31.72	6250	35.37
16200	0.4974	11250	33.01	6000	34.32
16100	0.8697	11000	34.19	5750	33.17
16000	1.302	10750	35.28	5500	31.94
15750	2.575	10500	36.25	5250	30.62
15500	4.052	10250	37.13	5000	29.23
15250	5.677	10000	37.89	4750	27.77
15000	7.407	9750	38.53	4500	26.24
14750	9.211	9500	39.06	4250	24.65
14500	11.07	9250	39.48	4000	23.02
14250	12.95	9000	39.77	3750	21.35
14000	14.85	8750	39.95	3500	19.65
13750	16.74	8500	40.01	3250	17.92
13500	18.62	8250	39.95	3000	16.19
13250	20.46	8000	39.77	2750	14.46
13000	22.25	7750	39.48	2500	12.75
12750	24.02	7500	39.07	2250	11.08
12500	25.71	7250	38.54	2000	9.453
12250	27.33	7000	37.91	1750	7.918
12000	28.87	6750	37.17	1500	6.512
11750	30.34	6500	36.32	1250	5.431

Table 6.2 – Photodetachment and Radiative Attachment Rates for H$^-$

T	Attachment	Detachment
100 K	1.04×10^{-16} cm^{3}s^{-1}	...
300 K	2.98×10^{-16}	3.08×10^{-9} s^{-1}
1000 K	8.51×10^{-16}	4.06×10^{1}
3000 K	1.89×10^{-15}	1.61×10^{5}
5800 K	2.77×10^{-15}	2.61×10^{6}
10000 K	3.61×10^{-15}	1.45×10^{7}

Let us therefore try to evaluate in more detail the dominant processes that govern the abundance of H^-. To a good first approximation, the state of the Sun's photosphere is well characterized by LTE. Thus,

$$\frac{n(\mathrm{H})n(e^-)}{n(\mathrm{H}^-)} \quad = \quad 4\left(2\pi mk\mathrm{T}/h^2\right)^{3/2} e^{-h\nu_\circ/k\mathrm{T}} \quad . \tag{6.6}$$

With $h\nu_\circ/k = 8762.67$ K and $(2\pi mk/h^2)^{3/2} = 2.42 \times 10^{15}$, we obtain for the same conditions as before $n(\mathrm{H}^-) = 2.0 \times 10^9$ cm^{-3}.

The removal rate of H^- through reaction (6.3) is $(2 \times 10^{-9}) \cdot (9.2 \times 10^{16}) = 1.8 \times 10^8$ s^{-1}. What formation rate is required to balance this removal rate?

$$n(\mathrm{H}^-)1.8 \text{ x } 10^8 \quad = \quad n(e^-)n(\mathrm{H})k_f \quad , \tag{6.7}$$

so $k_f \sim 1 \times 10^{-13}$ cm^{3}s^{-1}, nearly two orders of magnitude larger than the radiative attachment rate. The rapid formation process in this case is actually the *three body association* reaction

$$e^- \quad + \quad \mathrm{H} \quad + \quad \mathrm{H} \quad \to \quad \mathrm{H}^- \quad + \quad \mathrm{H} \quad , \tag{6.8}$$

which has a rate coefficient of 2.1×10^{-30} cm^{6}s^{-1}.

Given this abundance of H^- in the Sun's photosphere, let's see whether it is really important in terms of absorbing and reprocessing sunlight. The probability of absorption of a visible photon is governed by the optical depth τ according to $d\tau \sim n(\mathrm{H})\sigma_\nu dh$, where dh is an element of height through the photosphere.

It is useful at this point to approximate by $\tau_\mathrm{H} \sim n(\mathrm{H}^-)\sigma_\nu H_P$ for one pressure scale-height in the atmosphere, where

$$H_P^{-1} \quad = \quad \frac{1}{P}|dP/dr| \quad . \tag{6.9}$$

Using the fact that the Sun is evidently a system in hydrostatic equilibrium, i.e. in a situation where pressure force = gravitational force, one finds

$$H_P^{-1} \quad = \quad \frac{G\rho}{P}\frac{M_\odot}{R_\odot} \quad = \quad 5.6 \times 10^{-8} \text{ cm}^{-1} \quad , \tag{6.10}$$

or $H_P \sim 1.8$ x 10^7 cm = 177 km. Thus,

$$\tau_{H_P} \quad \sim \quad n(\mathrm{H}^-)\sigma_\nu H_P \quad \sim \quad 2 \times 10^9 \cdot 10^{-17} \cdot 1.8 \times 10^7 \quad \sim \quad 0.35 \quad , \tag{6.11}$$

so that, indeed, this small amount of H^- ($H^-/\mathrm{H} = 2 \times 10^{-8}$) is a significant opacity source.

2. Ionized Regions of the Interstellar Medium

Fifty years ago, the interstellar medium was thought to consist of a uniform gas cloud of about 1 atom per cm^{-3} containing mostly H and He. We now know that the distribution of interstellar matter is highly inhomogeneous, and that it consists of at least three different phases. Since hydrogen in by far the most abundant element in the universe, the various

phases can be characterized conveniently by the form in which hydrogen appears: neutral H atoms (H I), ionized H^+ atoms (H II), or the molecule H_2. Terminology for the ISM now stands as follows:

(i) A Hot Coronal Phase, which has a temperature of about 10^6 K, a density $n \sim 10^{-3}$ cm^{-3}, and in which occurs, because of the high temperature, mainly in the form of H^+ (or H II). This hot gas occupies a large fraction of the volume of the ISM and is produced and maintained by supernova explosions. It forms an interconnecting "tunnel" system in which the colder regions (ii) and (iii) are embedded.

(ii) The Warm Neutral Medium, surrounded by the Warm Ionized Medium, which both have T$\sim 10^4$ K, $n \sim 0.2$ cm^{-3}, and which hydrogen is either in its neutral atomic form H or its ionized form H^+. These regions form the outer parts of phase (iii).

There also exist warm photoionized H II regions surrounding bright stars, such as the diffuse nebulae and the planetary nebulae of which we have seen spectra in the introduction. Diffuse nebulae surround young O and B stars, and have typical densities of $N(e) = n(H^+) \sim 10 - 10^4$ cm^{-3} and T$\sim$5000-15,000 K. The nearest objects are extended on the sky, and their masses lie between 100 and 10^4 M$_\odot$. Planetary nebulae are shells of gas that have been lost in the fairly recent past of the central stars. The stars are quite old and hot, T$_* \gtrsim 50,000$ K, and are rapidly evolving toward the white dwarf stage. They are usually denser than the diffuse nebulae, $n(e^-) \sim$100-10^6 cm^{-3} and warmer, T$\sim$10,000-20,0000 K. They are also much smaller with masses between 0.1 and 1 M$_\odot$.

(iii) The Cold Neutral Condensations, or "clouds." Traditionally, two different kinds of clouds are distinguished:

•The diffuse interstellar clouds, which do not entirely obscure the light from stars which lie behind them and which may thus be conveniently studied by their absorption lines at visible and ultraviolet wavelengths superposed on the spectra of background stars. Diffuse interstellar clouds have T$\sim$20-100 K, $n \sim$20-200 cm^{-3}, and hydrogen occurs mostly in atomic form, H, although or $n \gtrsim 200$ cm^{-3} the fraction of molecular hydrogen, H_2, can become substantial.

•The dense, or dark interstellar clouds, which are opaque at visible and UV wavelengths, and which can thus only be observed by molecular emission at radio, (sub)millimeter, and, in certain cases, infrared wavelengths. They generally have low temperatures, T$\lesssim$10-15 K, high densities, $n \sim 10^4$-10^5 cm^{-3}, and hydrogen mostly in molecular form, H_2. Clouds in which star formations occurs have internal sources of energy, resulting in higher temperatures, T$\sim$50 K, and densities up to 10^{10} cm^{-3}.

Of course, various transition regions occur between these phases in the ISM, but they tend to be small in volume. The structure of the ISM is sketched in Figure 6.1, taken from
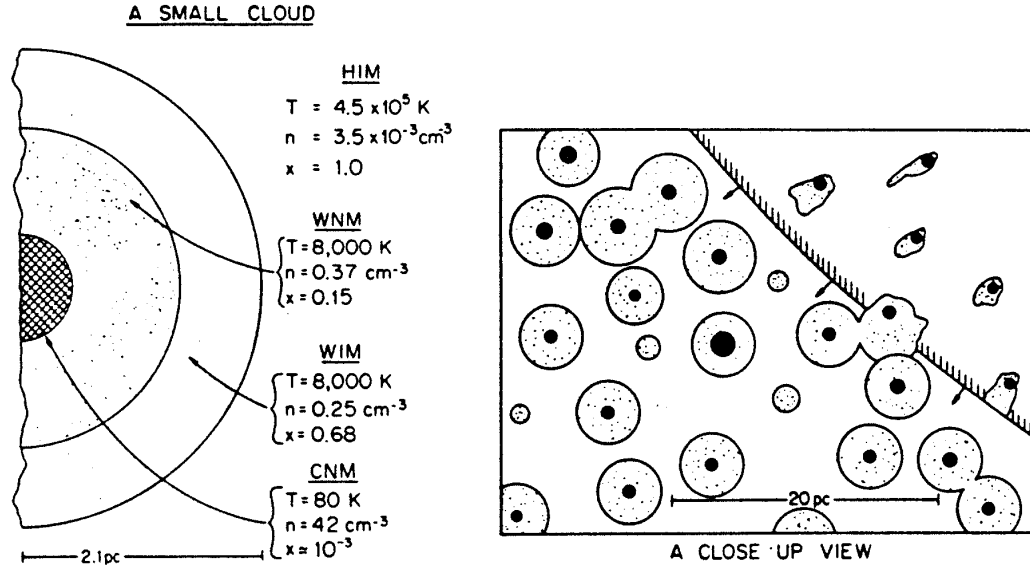
A SMALL CLOUD

HIM
T = 4.5 x 10^5 K
n = 3.5 x 10^{-3} cm^3
x = 1.0

WNM
T = 8,000 K
n = 0.37 cm^{-3}
x = 0.15

WIM
T = 8,000 K
n = 0.25 cm^{-3}
x = 0.68

CNM
T = 80 K
n = 42 cm^{-3}
x = 10^{-3}

2.1 pc

20 pc

A CLOSE UP VIEW

Figure 6.1– (Left) Cross section of a characteristic small cloud. The crosshatched region shows the cold core, which gives the usual optical absorption lines. Next is the warm neutral medium (WNM) with ionization produced by soft X-ray background. The outer layer (WIM) is gas largely ionized by stellar UV background. Typical values of the hydrogen density, n, temperature, T, and ionization $x = n_e/n$ are shown for each component. (Right) Small-scale structure of the interstellar medium (ISM). A cross section of a region 30 pc x 40 pc (pc = parsec = 3.2 light-years) in extent is shown, with the area of the features being approximately proportional to their filling factors. A supernova blast wave is expanding into the region from the upper right. The clouds inside the SNR (supernova remnant) are compressed and distored.

200 pc

A LARGE SCALE VIEW
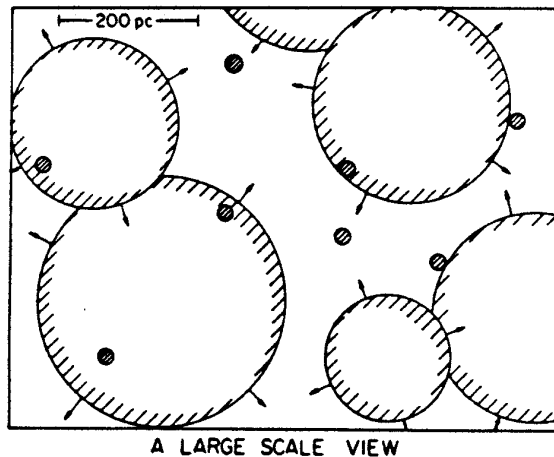
Large-scale structure of the ISM. The scale here is 20 times greater than at top left: The region is 600 × 800 pc. Only SNRs with $R < R_c = 180$ pc and clouds with $r_o > 7$ pc are shown. Altogether about 9000 clouds, most with warm envelopes with $r_w \sim 2.1$ pc would occur in a region this size.

McKee and Ostriker (1977, *Ap. J.* **218**, 148). In this section of *atomic processes*, we will focus mostly on the hot coronal phase and the nebulae.

(a) Photoionized Regions of the Interstellar Medium

(i) Structure of Nebulae

In diffuse and planetary nebulae, the ionization is due to photoionization by ultraviolet radiation from the star or stars in the nebula. The ionization equilibrium at each point in the nebula is determined by the balance between photoionization and recombination of electrons with ions. Consider first the structure of a pure hydrogen cloud surrounding a single hot star. The ionization equilibrium is:

$$n(\text{H})\Gamma_{pi}(\text{H}) \quad = \quad n(e^-)n(\text{H})^+\alpha_H \quad , \tag{6.12}$$

where α_H is the radiative recombination rate of hydrogen and Γ_{pi} is the photoionization rate

$$\Gamma_{pi} \quad = \quad \int_{\nu_\circ}^{\infty} \frac{4\pi I_\nu}{h\nu}\sigma_{pi}(\nu)d\nu \quad , \tag{6.13}$$

with I_ν the intensity in [ergs cm^{-2}s^{-1}Hz^{-1}sr^{-1}], σ_{pi} the photoionization cross section, and $h\nu_\circ$ the ionization potential.

The mean intensity $4\pi I_\nu$ is simply the radiation emitted by the star reduced by the inverse-square effect due to geometrical dilution:

$$4\pi I_\nu \quad = \quad \left(\frac{R_*}{R}\right)^2 \pi F_\nu(0) \quad = \quad \frac{L_\nu}{4\pi R^2} \quad , \tag{6.14}$$

where R_* is the radius of the star, $\pi F_\nu(0)$ is the flux at the surface of the star, and L_ν is the luminosity of the star per unit frequency interval. Usually, πF_ν is assumed to be a black-body spectrum at the effective temperature T_* of the star. Clearly, the higher T_*, the "harder" the spectrum, i.e. the more ultraviolet photons produced at shorter wavelengths (see Figure 6.2).

Using typical values of $T_* \sim 30,000$-$40,000$ K and $n \sim 10$ cm^{-3}, one can conclude from (6.12) that at distances close to the star ($R \sim 5$ pc $= 5 \cdot 3.086 \times 10^{18}$ cm), the fractional ionization $x = n(\text{H}^+)/\{n(\text{H}) + n(\text{H}^+)\}$ is nearly unity, i.e., H is nearly completely ionized.

On the other hand, it is clear that at a certain distance from the star, all the available ionizing photons have been absorbed, so that there must be an outer edge to the ionized material. That is, a finite source of UV photons cannot ionize an infinite volume. It can be shown that the thickness of this ionized/neutral transition zone, where $n(\text{H}) \sim n(\text{H}^+)$, is very small, namely

$$d \quad \sim \quad \frac{1}{\tau_\text{H} = 1} \quad = \quad \frac{1}{n(\text{H})\sigma_\text{H}} \quad \sim \quad 0.01 \text{ pc} \quad , \tag{6.15}$$

i.e., much smaller than the radius of the ionized nebula. Figure 6.3 illustrates this drop in fractional ionization for a hot O6 star with $T_* = 40,000$ K, and a somewhat cooler B0
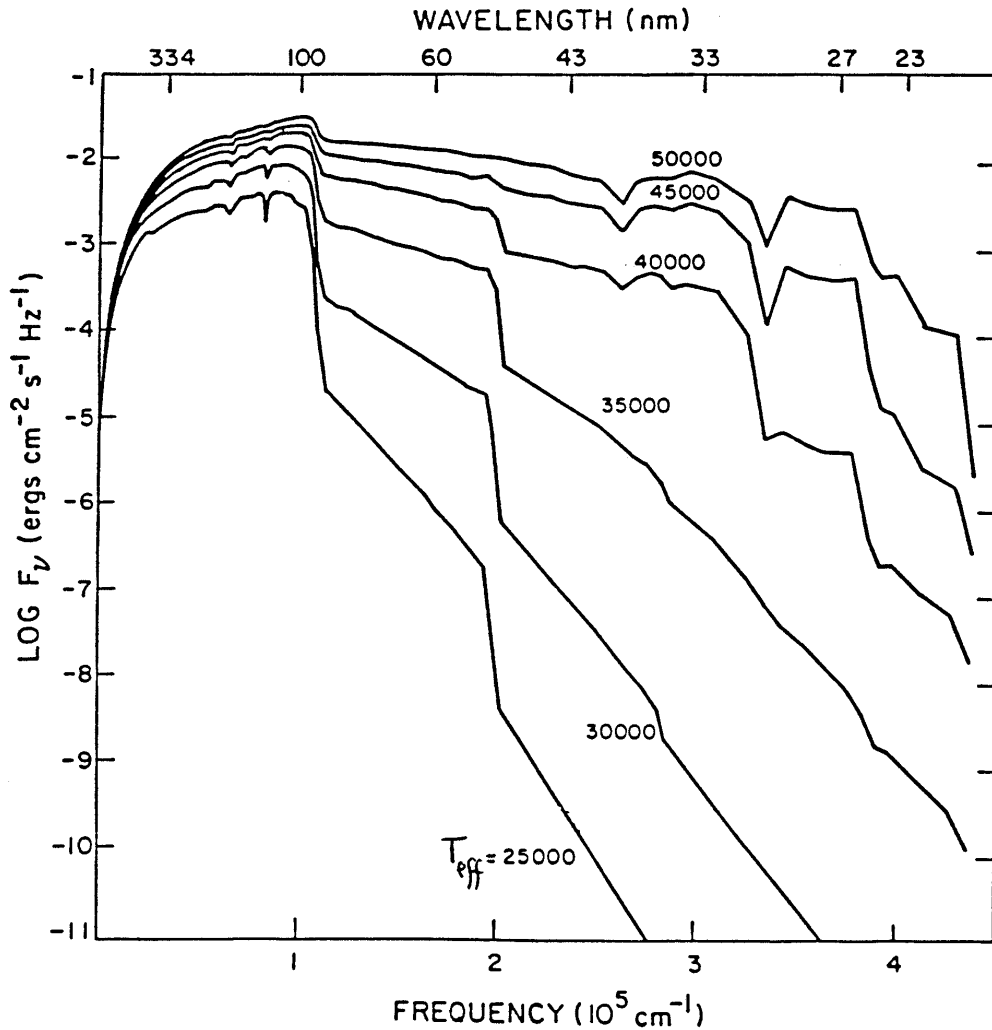
Figure 6.2– The energy flux F_ν is shown as a function of frequency ν for various effective temperatures. The fluxes are obtained from model calculations of atmospheres with a surface gravity of 10^5 dynes. In terms of F_ν, the luminosity is $L_\nu = 4\pi R_*^2(\pi F_\nu)$.

star for which the effective temperature is $T_* = 30{,}000$ K. The radius of the completely ionized region is called the *Stromgren radius*.

Consider now the photoionization of a nebula containing both hydrogen and helium. The ionization potential of He is 24.6 eV (504 Å), considerably higher than that of H, so that hotter stars are required to ionize He. The ionization potential of He^+ is 54.4 eV (photon wavelength 227.8 Å), but since even the hottest O stars emit practically no photons with $h\nu >$54.4 eV, the second ionization of He does not occur in ordinary H II regions. In planetary nebulae, however, the observation of He II recombination lines (resulting from $He^{++} + e^-$ recombination) is a strong indicator that the effective temperature of the ionization source must be very high indeed.

For normal central O and B stars, two possibilities can occur. First, if the spectrum peaks at energies just above 13.6 eV and has few photons at $h\nu >$24.6 eV, all photons
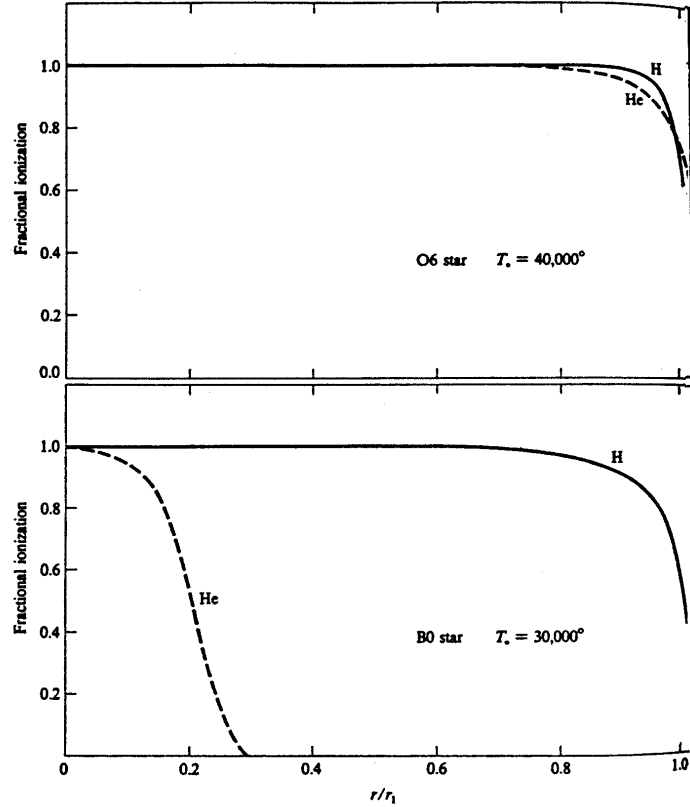
Figure 6.3– Ionization structure of two homogeneous H+He model H II regions ($r_1 =$ Stromgren radius).

Table 6.3 – Solar Elemental Abundances

Element	Abundance	Element	Abundance
H	1.00	Si	4.3(-5)
He	0.075	S	1.7(-5)
O	8.3(-4)	P	2.8(-7)
C	4.0(-4)	Cl	1.1(-7)
N	1.0(-4)	K	1.3(-7)
Na	2.1(-6)	Ca	2.2(-6)
Mg	4.2(-5)	Fe	4.3(-5)
Al	3.1(-6)	...	...

with $13.6 < h\nu < 24.6$ eV will ionize H, whereas the photons with $h\nu > 24.6$ eV ionize He (remember that at high energies, He is a more effective absorber of photons than hydrogen, see §IV.A.2). Thus, the structure will consist of a small central He^+ zone, surrounded by a larger H^+ region (Figure 6.3, bottom). On the other hand, if the input spectrum contains many photons with $h\nu > 24.6$ eV, then these photons dominate the ionization of *both* H and He, and the outer boundaries of the two ionized zones will approximately coincide (Figure 6.3, top).
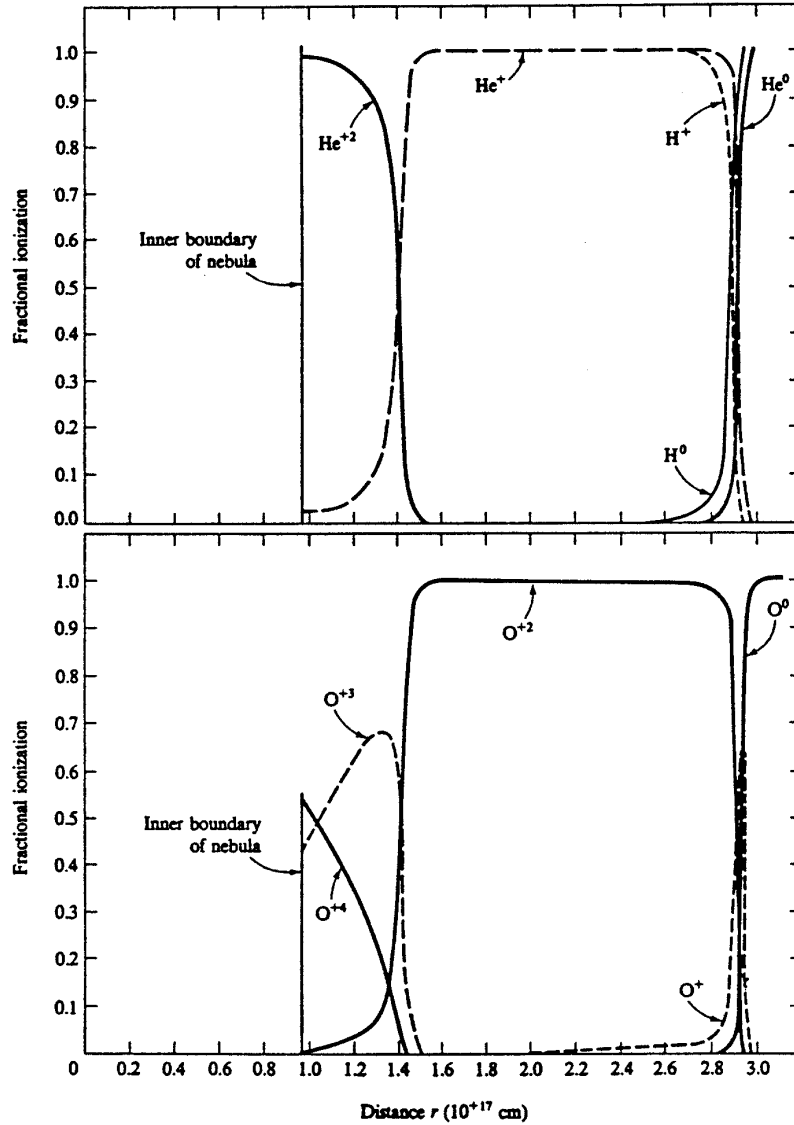
Figure 6.4– The ionization structure of H, He (top), and O (bottom) atoms for a model planetary nebula.

Note that the photoionization of He is balanced by the recombination of He^+ back to He. As we have seen (§IV), the recombinations into the excited states of He eventually lead to population of either the $2\ ^1S$, $2\ ^1P$, or the $2\ ^3S$ states. If the density of the nebula is low, $n(e^-) \lesssim 3300$ cm^{-3}, the $2\ ^3S$ state will decay by emission of a photon at 19.8 eV. The $2\ ^1P$ state radiates rapidly to the $1\ ^1S$ state by the resonance transition at 21.2 eV, whereas the $2\ ^1S$ state decays through the two-photon process (remember the J = 0 to J = 0 selection rules). As illustrated in Figure 3.2, the two-photon emission peaks around 800 Å and on average 56% of the emitted photons have an energy $h\nu >$13.6 eV. Thus, with the exception of a small fraction of the events ending in the $2\ ^1S$ state, all photons resulting from the recombination of He^+ and e^- can ionize hydrogen. The presence of He in the nebula therefore does *not* affect the ionization structure of hydrogen.

A similar analysis can be carried out for the ionization of the "heavy" elements O, Ne, C, N, Fe, Si, ... in the nebula. Because the abundances of these species are small compared with hydrogen (Table 6.3), they do not affect the ionization of H or He. Figure 6.4 illustrates the ionization structure of H, He (top), and O (bottom) for a model planetary nebula with $T_* = 10^5$ K. Photons with high energies are needed to produce the higher ionization stages of oxygen. Note that there is a substantial zone of O^{3+} coincident with the region where He^{++} is dominant. This results from the fact that the ionization potential of O^{++} is 54.9 eV, nearly the same as that of He^+.

As mentioned in §V.6, charge transfer processes can affect the ionization equilibrium of some elements such as oxygen, especially near the outer boundaries where there is a large fraction of neutral hydrogen.

(ii) Thermal Balance

The steady state kinetic temperature of the gas T in the interstellar medium is governed by the rate at which absorbed radiation is converted to kinetic energy (*heating*) and the rate at which kinetic energy of the gas is converted into radiation that escapes (*cooling*).

Photoionization by a photon of energy $h\nu$ produces an electron with excess kinetic energy $(h\nu - h\nu_\circ)$, so the heating rate is

$$G_{pi} = \int_0^\infty 4\pi I_\nu \frac{\nu - \nu_\circ}{\nu} \sigma_{pi}(\nu) d\nu \quad . \tag{6.16}$$

Thus, the electrons are "created" with this energy; subsequent elastic collisions with other species in the gas rapidly thermalize the electrons. In ionization equilibrium, the photoionizations are balanced by radiative recombination. In each recombination, a thermal electron with energy $mv^2/2$ disappears. The resulting cooling rate for, for example, hydrogen, is

$$L_R = n(e^-)n(H^+)kT\beta(H,T) \quad , \tag{6.17}$$

where β is an effective kinetic-energy averaged recombination rate coefficient

$$\beta = \sum_n \frac{1}{kT} \int_0^\infty v\sigma_n(H,T)\frac{1}{2}mv^2 f(v)dv \quad . \tag{6.18}$$

In a pure hydrogen nebula, the thermal equilibrium equation would be:

$$G_{pi}(H) = L_R(H) \quad . \tag{6.19}$$

In a real nebula, additional cooling occurs by free-free emission (or *bremsstrahlung*) and, more importantly, by collisional excitation of bound levels of heavy species followed by radiative decay. The cooling due to free-free emission is:

$$L_{FF} = 1.42 \times 10^{-27}T^{1/2}g_{ff}n(e^-)n(H^+) \quad , \tag{6.20}$$

where the Gaunt factor g_{FF} is of order unity, 1.0< g_{ff} <1.5.

The most important source of radiative cooling is collisional excitation of low-lying energy levels of common ions such as O^+, O^{++}, N^+, ... followed by emission of a photon that can escape from the nebula. The reason that these heavy atoms are so effective in the cooling in spite of their small abundance is that they have low-lying energy levels at or near $\Delta E \sim$ 1-2 eV $\sim kT$ for T$\sim$10000 K. In contrast, the lowest excited states of H and He lie at $\Delta E >$ 10.2 eV.

In order to calculate the cooling rates for these heavy atoms, consider the case of a species with a ground state level 1 and a singly excited level 2. In the limit of very *low electron density*, every collisional excitation is followed by the emission of a photon, so that the cooling rate is

$$L_C = n_{e^-} n_1 q_{12} h\nu_2 \ , \tag{6.21}$$

where q_{12} is the collisional excitation rate coefficient due to electrons. If the density is sufficiently high, collisional de-excitation will start to become as fast as radiative decay. Thus, every collision no longer produces a photon, and the cooling rate is reduced. The equilibrium equation for the balance between excitation and de-excitation can be written as

$$n_{e^-} n_1 q_{12} = n_{e^-} n_2 q_{21} + n_2 A_{21} \ , \tag{6.22}$$

$$\text{so} \qquad \frac{n_2}{n_1} = \frac{n_{e^-} q_{12}}{A_{21}} [1 + \frac{n_{e^-} q_{21}}{A_{21}}]^{-1} \ . \tag{6.23}$$

The cooling rate is therefore

$$L_C = n_2 A_{21} h\nu_{21} \ . \tag{6.24}$$

For low densities, $n_{e^-} q_{21} << A_{21}$, this formula reduces to (6.21). For $n_{e^-} \to \infty$, the relative populations get into thermodynamic equilibrium, and

$$L_C \to n_1 \frac{g_2}{g_1} e^{-\Delta E/kT} A_{21} h\nu_{21} \ . \tag{6.25}$$

This simple analysis for a two-level system is easily generalized to atoms with more levels. The equations of statistical equilibrium become:

$$\sum_{j \neq i} n_j n_{e^-} q_{ji} + \sum_{j > i} n_j A_{ji} = \sum_{j \neq i} n_i n_{e^-} q_{ij} + \sum_{j < i} n_i A_{ij} \ , \tag{6.26}$$

subject to the condition $\sum_j n_j = n$. These equations can be solved analytically by straightforward algebra, but the analysis rapidly becomes very tedious (and you thought equivalent electrons were messy!). It is much simpler in those cases to solve the equations numerically. Once the populations of each level have been determined, the cooling rate can be found from

$$L_C = \sum_i n_i \sum_{j < i} A_{ij} h\nu_{ij} \ . \tag{6.28}$$

In the low-density limit, L_C becomes a sum of terms like (6.21), but for higher densities collisional excitation is not negligible and the complete solution must be used. For any level i, a *critical density* $n_{cr}(i)$ can be defined as:

$$n_{cr}(i) = \sum_{j < i} A_{ij} / \sum_{j \neq i} q_{ij} \ , \tag{6.29}$$

so that for $n_{e-} < n_{cr}(i)$, collisional de-excitation of level i is negligible, but for $n_{e-} > n_{cr}(i)$ this process is important. Critical densities for a number of important species and transitions are listed in Table 6.4.

The thermal balance thus becomes

$$G_{pi} = L_R + L_{FF} + L_C \quad \text{or} \quad G - L_R = L_{FF} + L_C \;, \qquad (6.30)$$

where $G - L_R$ is the "effective heating rate", representing the net energy gained via the photoionization process with the recombination losses already subtracted. Note that at low densities, all terms are proportional to $n(e^-)$, so that the temperature is independent of density. It does, of course, depend on the abundances of the heavy species. If they are depleted from the gas phase, the cooling will be reduced significantly and much higher temperatures can result. The heating and cooling rates are illustrated in Figure 6.5 for various models atmospheres. The temperature then folows from the point at which the heating and cooling curves cross. Note that this temperature is rather insensitive to the input radiation field – temperatures ranging between 7,000 and 13,000 K are obtained for a wide range of conditions. The main coolant appears to be the [O II] ^{4}S – ^{2}D lines at 3729 and 3726 Å, and these lines are indeed prominently observed in nebulae.

Table 6.4 – Critical Densities for Collisional De-excitations at T = 10^4 K

Ion	Level	N_c(cm^{-3})	Ion	Level	N_c(cm^{-3})
C II	$^2P_{3/2}$	8.5×10^1	O III	$^1D_2$	7.0×10^5
			O III	$^3P_2$	3.8×10^3
C III	$^3P_2$	5.4×10^5	O III	$^3P_1$	1.7×10^3
N II	$^1D_2$	8.6×10^4	Ne II	$^2P_{1/2}$	6.6×10^5
N II	$^3P_2$	3.1×10^2			
N II	$^3P_1$	1.8×10^2	Ne III	$^1D_2$	7.9×10^6
			Ne III	$^3P_0$	2.0×10^4
N III	$^2P_{3/2}$	3.2×10^3	Ne III	$^3P_1$	1.8×10^5
N IV	$^3P_2$	1.4×10^6	Ne V	$^1D_2$	1.6×10^7
			Ne V	$^3P_2$	3.8×10^5
O II	$^2D_{3/2}$	1.6×10^4	Ne V	$^3P_1$	1.8×10^5
O II	$^2D_{5/2}$	3.1×10^3			

For high densities, $n_{e-} > n_{cr} \sim 10^4$ cm^{-3}, collisional de-excitation becomes important, so that the cooling is reduced which results in higher temperatures.

(iii) Spectra of Nebulae

What do the spectra of these nebulae look like? What is the mechanism for producing the observed lines? What can we learn from them? The envelop please!...

irst of all, it is clear that the *recombination* processes following photoionization result in the emission of photons. The initial recombination "free→bound" step produces a *continuum* of radiation, whereas the subsequent cascade from the higher to the lower atomic levels produces *discrete* photons. These recombination lines are prominently observed for H and He in all nebulae at optical, infrared, and radio wavelengths (see e.g. Figures in the
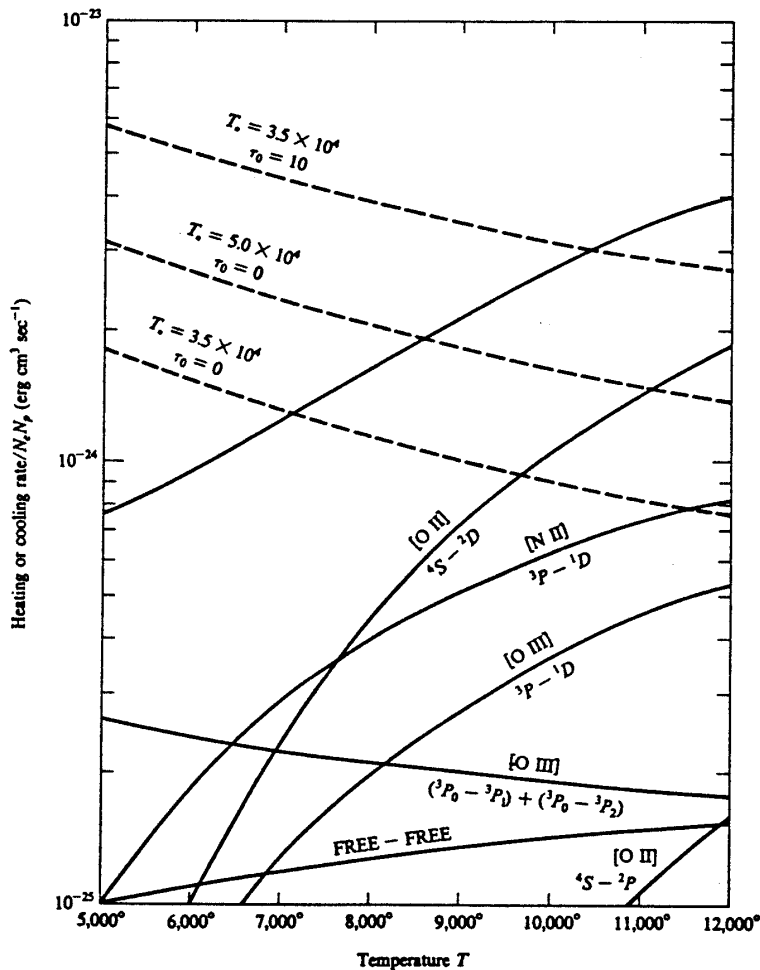
Figure 6.5– Net effective heating rates $(G - L_R)$ for various stellar input spectra, shown as dashed curves. Total radiative cooling rate $(L_{FF} + L_C)$ for the simple approximation to the H II region of the kind described in the text is shown as the highest solid black curve, and the most important individual contributors to radiative cooling are shown by labeled solid curves. The equilibrium temperature is given by the intersection of a dashed curve and the highest solid curve. Note how the increased optical depth τ_0 or increased stellar temperature T_* increases T by increasing G.

Introduction). The theory of the formation of recombination lines is straightforward, but tedious, because of radiative transfer effects, and will therefore not be presented here. For more information you should consult sources such as Osterbrock Ch. IV; B.T. Lynds and R.L. Brown in *Spectroscopy of Astrophysical Plasmas* Ch. 1 and 2; and Brown, Lockman, and Knapp 1978, *Ann. Rev. Astron. Ap.* **16**, 445.

As noted before, observations of He II recombination lines indicate a rather hot ionization source. Also, as we have seen, observations of charge-transfer recombination lines such as the O^{2+} 5592 Å line demonstrate the co-existence of multiply-charged ions and neutral material – and are thus another indication that the ionization is produced by a

high-excitation source. By comparing the strength of emission lines of the next ionization stage with those of a line due to charge-transfer recombination, the fractional *neutral content* in the ionized zone can be determined, since

$$\frac{I_1}{I_2} \quad \propto \quad \frac{n_{e^-} n(\mathrm{X}^{m+1})}{n(\mathrm{X}^{m+1}) n(\mathrm{H})} \quad \propto \quad \frac{n_{e^-}}{n(\mathrm{H})} \quad . \tag{6.31}$$

The recombination lines of heavier species are usually too weak to be observed, although one exception will be presented in §VI.3.

The lines of the heavier species that are quite prominently observed in nebulae are the forbidden emission lines at visible and infrared wavelengths (again, see the Figures in the Introduction), and the electric dipole allowed transitions at ultraviolet wavelengths. The forbidden lines result from *collisional excitation*, followed by radiative decay. Since this same process is responsible for the cooling of the nebula, observations of the strength of the emission lines are a direct measure of the cooling in the nebula. More importantly, suitably chosen ratios of line strengths can be used as *diagnostics* of the *temperature and density* in the nebula. Finally, once these physical conditions are known, the *abundances* of the species can be determined from the observed line strengths.

Below we discuss the use of atomic lines as diagnostics in more detail.

(iv) Temperature Measurements from Emission Lines

The temperature in a nebula can be determined most easily from measurements of the ratio of the intensity of pairs of emission lines arising from two levels of a single ion with considerably different excitation energies. The best examples are [O III] and [N II], since their lines occur in the visible wavelength region. As Figure 5.7 shows, the [O III] $\lambda 4959$ and $\lambda 5007$ Å lines come from the intermediate ^{1}D level. It is clear that the relative rates of excitation to the ^{1}S and ^{1}D levels depend very strongly on T, so the relative strengths of the lines emitted by these levels may be used to measure the electron temperature.

To compute the relative strengths exactly, we would have to solve the equations (6.26) for the populations of the various levels, and then compute line intensities from

$$I_\nu \quad = \quad \frac{n_2 A_{21} h \nu_{21}}{4\pi} \quad . \tag{6.32}$$

Let us look as an *example* at the case of O III. Figure 6.6 summarizes all the relevant atomic data for this system. For some of the transitions indicated, *multiplet* collision strengths are shown. In these cases, whenever S = 0 or L = 0, the values for the individual transitions are given by

$$\Omega(\mathrm{SLJ}, \ \mathrm{S'L'J'}) \quad = \quad \frac{(2\mathrm{J'} \ + \ 1)}{(2\mathrm{S'} \ + \ 1)(2\mathrm{L'} \ + \ 1)} \ \Omega_\mathrm{M}(\mathrm{SL}, \ \mathrm{S'L'}) \quad . \tag{6.33}$$

Recall that the collisional de-excitation rates are

$$q_{ul} \quad = \quad 8.629 \times 10^{-6} \mathrm{T}^{-1/2} \frac{\Omega(l, u)}{g_u} \quad , \tag{6.34}$$
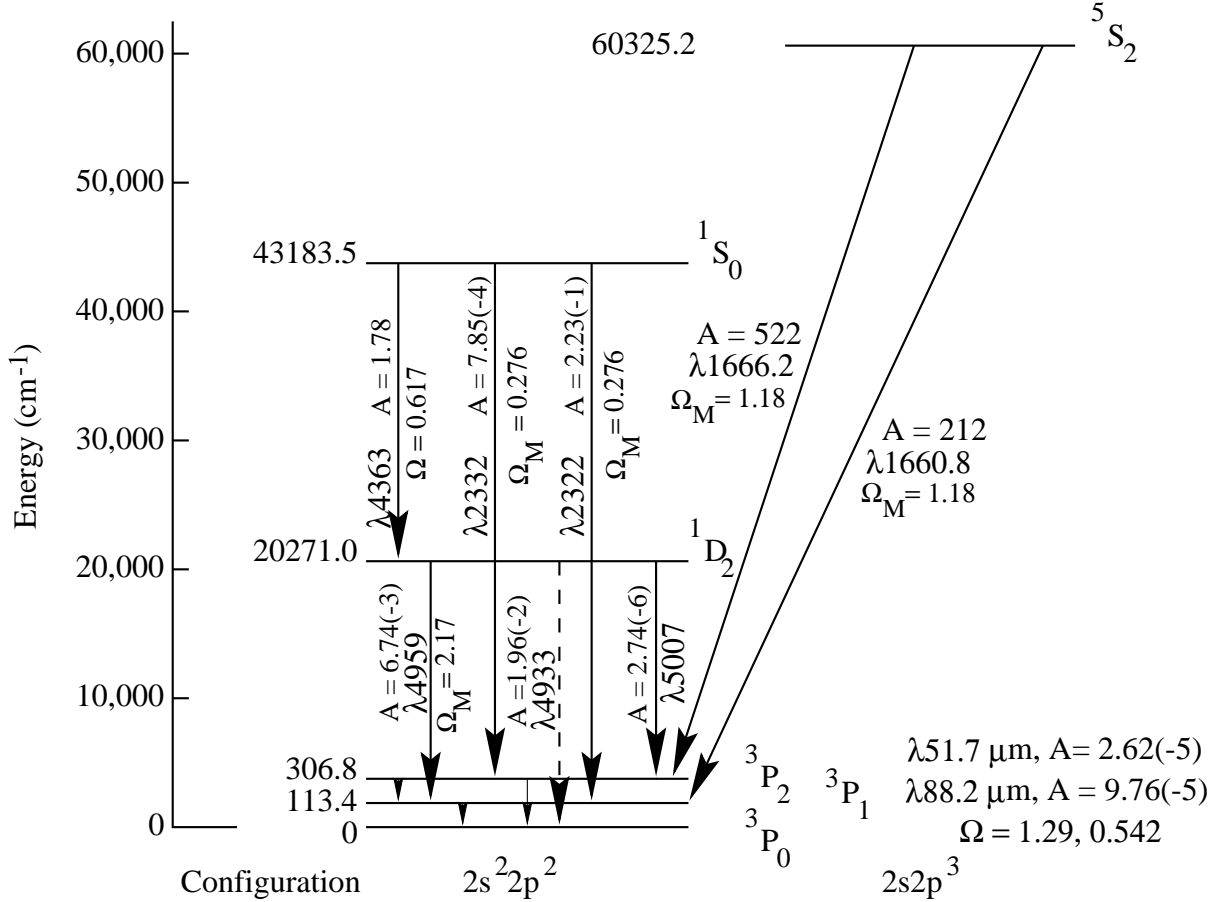
Figure 6.6– The O III ion: E in cm^{-1}, λ in Å unless marked as μm, A-values in s^{-1}. As before, $7.85(-4) \rightarrow 7.85 \times 10^{-4}$. For collision strengths, Ω_M indicates "multiplet" values.

with $g_u = 2J_u + 1$. The listed values of Ω for O III are appropriate for T $= 10^4$ K, but are quite insensitive to T in the range 5,000-30,000 K.

First for ^{1}D$_2 - ^3$P$_1$, let us compare collisional and radiative de-excitation rates:

$$n(e^-)q_{ul} \quad \sim \quad n(e^-)2.08 \times 10^{-8} \quad [\text{s}^{-1}]$$

$$A \quad = \quad 6.74 \times 10^{-3} \quad [\text{s}^{-1}].$$

This means that these rates are comparable at $n_{cr} \sim 3.2 \times 10^5$ cm^{-3}. At lower densities, spontaneous emission dominates. The steady-state concentration in, e.g. ^{1}D$_2$ is thus:

$$n(^1\text{D}_2)[\text{A}(^1\text{D}_2 -^3 \text{P}_2) + \text{A}(^1\text{D}_2 -^3 \text{P}_1) + \text{A}(^1\text{D}_2 -^3 \text{P}_0)$$

$$+ n(e^-)(q_M(^1\text{D}_2 -^3 \text{P}) + q(^1\text{D}_2 -^1 \text{S}_0))] \quad =$$

$$n(e^-)[n(^3\text{P}_0)q(^3\text{P}_0 -^1 \text{D}_2) + n(^3\text{P}_1)q(^3\text{P}_1 -^1 \text{D}_2) + n(^3\text{P}_2)q(^3\text{P}_2 -^1 \text{D}_2)]$$

$$+ n(^1\text{S}_0)[q(^1\text{S}_0 -^1 \text{D}_2)n(e^-) + \text{A}(^1\text{S}_0 -^1 \text{D}_2)] \qquad (6.35)$$

– 118 –

There are, of course, similar equations for each of the other level populations. It is likely that the ^{3}P fine structure levels are populated according to their statistical weights at high temperatures, and that the ^{1}S$_0$ level, which lies much higher in energy, is significantly less populated. Thus, we are left with the equation

$$n(^1\mathrm{D}_2)[\mathrm{A}(^1\mathrm{D}-^3\mathrm{P}) \;+\; n(e^-)\{q(^1\mathrm{D}-^3\mathrm{P}) \;+\; q(^1\mathrm{D}-^1\mathrm{S}\}] \quad \sim \quad n(e^-)n(^3\mathrm{P})q(^3\mathrm{P}-^1\mathrm{D}_2) \;.$$
(6.36)

From Figure 6.6 we derive

$$q(^1\mathrm{D}_2-^1\mathrm{S}_0) = 0.12e^{-32967.19/\mathrm{T}} \cdot 8.63 \times 10^{-6}\mathrm{T}^{-1/2} = 1.065 \times 10^{-6}T^{-1/2}e^{-32967.2/\mathrm{T}}$$

$$q(^1\mathrm{D}_2-^3\mathrm{P}) \quad = \quad 8.629 \times 10^{-6}\mathrm{T}^{-1/2}\frac{\Omega_M}{(2\mathrm{S}_u+1)(2\mathrm{L}_u+1)} \quad = \quad 3.745 \times 10^{-6}\mathrm{T}^{-1/2}$$

$$q(^3\mathrm{P}-^1\mathrm{D}) \quad = \quad \frac{(2\mathrm{S}_u+1)(2\mathrm{L}_u+1)}{(2\mathrm{S}_l+1)(2\mathrm{L}_l+1)}q(^1\mathrm{D}_2-^3\mathrm{P})e^{-28866.89/\mathrm{T}}$$

$$\sim 2.081 \times 10^{-6}\mathrm{T}^{-1/2}e^{-28866.89/\mathrm{T}}$$

$$\mathrm{A}(^1\mathrm{D}-^3\mathrm{P}) \quad = \quad \sum_J[\mathrm{A}(^1\mathrm{D}_2-{}^3\mathrm{P}_J)] \quad = \quad 2.34 \times 10^{-2} \quad [\mathrm{s}^{-1}]$$

Thus, if $n(^3\mathrm{P})\sim n(\mathrm{O}^{++})$, i.e., if most of the O^{++} ion is in its ground state, then the line intensity becomes

$$I(4959+5007+4933) \quad \propto \quad n(^1\mathrm{D}_2)\mathrm{A}(^1D-^3P)$$

$$\sim \quad \frac{n(\mathrm{O}^{++})n(e^-)2.08 \times 10^{-6}\mathrm{T}^{-1/2}e^{-28866.89/\mathrm{T}}}{1 + 4.043 \times 10^{-5}n(e^-)\mathrm{T}^{-1/2}[3.516 + e^{-32967.19/\mathrm{T}}]}$$
(6.37)

Note that when $n(e^-) << 7 \times 10^5$, $I \propto n(e^-)$, but when $n(e^-) >> 7 \times 10^5$, I is independent of $n(e^-)$. The dominant T dependence is

$$I \quad \propto \quad \mathrm{T}^{-1/2}e^{-28866.89/\mathrm{T}} \quad .$$
(6.38)

Although it is possible to solve the population equations for each level, it is simpler and more instructive to proceed by direct physical reasoning. In the low density limit (collisional de-excitations negligible), every excitation to the ^{1}D level results in the emission of a photon either at $\lambda5007$ or $\lambda4959$ Å, with relative probabilities given by the ratio of the two transition probabilities, which is very close to 3 to 1 (see Figure 6.6). Every excitation of ^{1}S is followed by the emission of a photon at either $\lambda4363$ or $\lambda2321$ Å, with the relative probabilities again given by the transition probabilities, about 9 to 1. Each emission of a photon at 4363 Å further results in the population of ^{1}D, which again is followed by emission of photons with wavelengths $\lambda4959$ or $\lambda5007$ Å. However, this is a small contribution to the total emission of ^{1}D, since even at high temperatures $\Omega(^3\mathrm{P}, {}^1\mathrm{S})\sim0.13\Omega(^3\mathrm{P}, {}^1\mathrm{D})$. Thus,

$$\frac{I_{4959}+I_{5007}}{I_{4363}} \quad \sim \quad \frac{\Omega(^3\mathrm{P},{}^1\mathrm{D})}{\Omega(^3\mathrm{P},{}^1\mathrm{S})}\left[\frac{\mathrm{A}(^1\mathrm{S},{}^1\mathrm{D}) + \mathrm{A}(^1\mathrm{S},{}^1\mathrm{D})}{\mathrm{A}(^1\mathrm{S},{}^3\mathrm{P})}\right]\frac{\nu(^3\mathrm{P},{}^1\mathrm{D})}{\nu(^3\mathrm{P},{}^1\mathrm{S})}e^{-\{\mathrm{E}(^1\mathrm{D}_2) - \mathrm{E}(^1\mathrm{S}_0)/k\mathrm{T}\}}$$
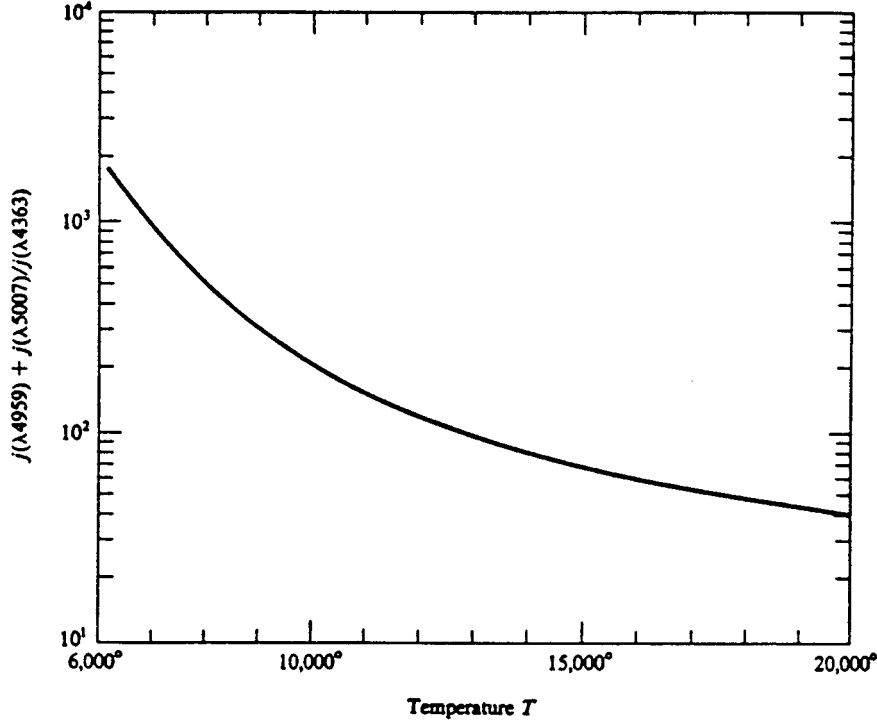
Figure 6.7– [O III] ($\lambda 4959$ + $\lambda 5007$)/$\lambda 4363$ intensity ratio in the low density limit as a function of T.

$$\sim \quad \frac{2.17}{0.276} \left[\frac{1.78 + 0.23 \frac{20021}{22913}}{1.78} \right] e^{32967/\mathrm{T}} \tag{6.39}$$

$$\text{or} \quad \frac{I_{4959} + I_{5007}}{I_{4363}} \quad \sim \quad 7.76 \; e^{32967/\mathrm{T}} \tag{6.40}$$

Figure 6.7 illustrates the intensity ratio as a function of temperature in the low density limit. At higher densities ($n(e^-) \gtrsim 10^5$ cm^{-3}), collisional de-excitation starts to play a role. The lower ^{1}D term has a much longer radiative lifetime than the ^{1}S term, so it is collisionally de-excited at lower electron densities than ^{1}S, thus weakening the 4959 and 5007 Å lines with respect to $\lambda 4343$ Å. In this case, we have to use the full statistical equilibrium equations (6.35), and to first order we can write (c.f. (6.37)):

$$\frac{I_{4959} + I_{5007}}{I_{4363}} \quad \sim \quad \frac{7.76 \; e^{32967/\mathrm{T}}}{1 + 4.5 \times 10^{-4}(n(e^-)/\mathrm{T}^{1/2})} \quad . \tag{6.41}$$

A similar analysis may be carried out for [N II] with the result:

$$\frac{I_{6548} + I_{6583}}{I_{5755}} \quad \sim \quad \frac{6.91 \; e^{25000/\mathrm{T}}}{1 + 2.5 \times 10^{-3}(n(e^-)/\mathrm{T}^{1/2})} \quad . \tag{6.42}$$

Note that because the lines are electric dipole forbidden, they are optically thin, so that no correction for radiative transfer needs to be applied to the ratio. Also, if the lines

lie close together in wavelength, the correction due to interstellar extinction will be very small.

Figure 6.7 shows that the [O III] line intensity ratio $I_{4959} + I_{5007}/I_{4363}$ is quite large (about 100), and is therefore difficult to measure accurately. Although the 4959 and 5007 Å lines are very strong in many nebulae the 4363 Å line is relatively weak, and furthermore is close to the Hg I 4358 Å line; which unfortunately is becoming stronger and stronger in the spectrum of the sky (Why?). Also, large intensity ratios are difficult to measure accurately in general, unless the sensitivity of the detector is very well calibrated (as is the case for CCD spectrographs).

Table 6.5 compares the temperature determinations for the O III and N II ratios for a number of planetary nebulae. In general, the agreement is quite good. For planetary nebulae, the temperatures lie in the range 9,000-13,000 K; for diffuse nebulae they are slightly lower, some 7,000-13,000 K.

<div align="center">

Table 6.5 – Temperature Determinations for Planetary Nebulae

Nebula	T[N II] (° K)	T[O III] (° K)
NGC 650	9,500	10,700
NGC 4342	10,100	11,300
NGC 6210	10,700	9,700
NGC 6543	9,000	8,100
NGC 6572	—	10,300
NGC 6720	10,600	11,100
NGC 6853	10,000	11,000
NGC 7027	—	12,400
NGC 7293	9,300	11,000
NGC 7662	10,600	12,800
IC 418	—	9,700
IC 5217	—	11,600
BB 1	10,500	12,900
Haro 4-1	—	12,000
K 648	—	13,100

</div>

(v) Electron Densities from Emission Lines

The average electron density in a nebula may be measured by observing the effects of collisional de-excitation. To do this, the intensities of two lines of a given ion emitted by
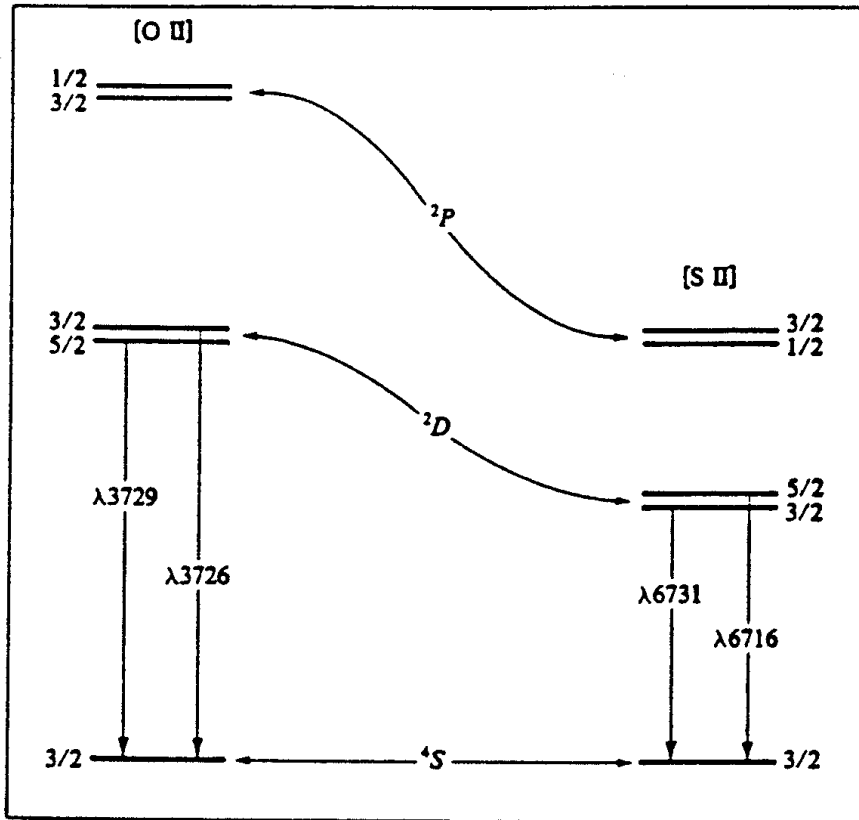
Figure 6.8– Energy level diagrams of the $2p^3$ ground configuration of [O II] and $3p^3$ ground configuration of [S II].

different levels with nearly the same excitation energy are compared, so that the relative excitation rates of the two levels depend only on the ratio of the collision strengths. If the two levels have different radiative transition probabilities or different collisional de-excitation rates, the relative populations of the two levels are density sensitive, and the ratio of the intensities they emit will likewise depend on the density. The best examples of lines that may be used to measure the electron density are [O II] $\lambda3729/\lambda3726$ Å and [S II] $\lambda6716/\lambda6731$ Å, for which the energy-level diagrams are shown in Figure 6.8.

The relative populations of the various levels and the resulting line intensities may be found in the same way as before, by setting up the statistical equilibrium equations (6.26). However, direct physical reasoning easily shows what effects are involved.

Consider the example of [O II] in the low density limit, that is for $n(e^-) \rightarrow 0$, in which every collisional excitation is followed by the emission of a photon. Since the relative excitation rates of the $^2D_{5/2}$ and $^2D_{3/2}$ levels are proportional to their statistical weights (see equation 6.33), the ratio of strengths of the two lines is simply

$$I_{3729}/I_{3726} = 1.5 \quad . \tag{6.43}$$

In the high-density limit, $n(e^-) \rightarrow \infty$, collisional excitations and de-excitations dominate and set up a Boltzmann population ratio for the two levels. Thus, the relative populations
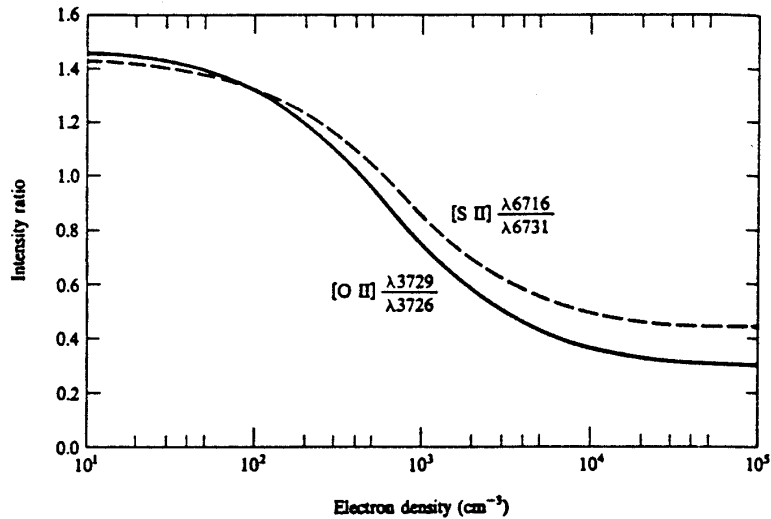
Figure 6.9– Calculated variation of [O II] (*solid line*) and [S II] (*dashed line*) intensity ratios as a function of $n(e^-)$ at T $= 10^4$ K. At other temperature the plotted curves are very nearly correct if the horizontal scale is taken to be $n(e^-)(10^4/\text{T})^{1/2}$ cm^{-3}K$^{-1/2}$.

of the two levels $^2\text{D}_{5/2}$ and $^2\text{D}_{3/2}$ are in the ratio of their statistical weights, and therefore the relative strengths of the two lines are in the ratio

$$\frac{I_{3729}}{I_{3726}} = \frac{n(^2\text{D}_{5/2})}{n(^2\text{D}_{3/2})}\frac{\text{A}_{3729}}{\text{A}_{3726}} = \frac{3}{2}\frac{3.6 \times 10^{-5}}{1.8 \times 10^{-4}} = 0.30 \quad . \tag{6.44}$$

Thus, the ratio of the line strengths will change from 1.5 to 0.3 with increasing density, and the largest change occurs in the neighborhood of the critical densities, which are $n_{cr} \sim 3 \times 10^3$ cm^{-3} for $^2\text{D}_{5/2}$ and $n_{cr} \sim 1.6 \times 10^4$ cm^{-3} for $^2\text{D}_{3/2}$. The result of the full solution of the statistical equilibrium equations, which includes excitation to the ^2P levels with subsequent cascading downward, is plotted in Figure 6.9. Note that through the collisional rates, the ratio depends mainly on $n(e^-)\text{T}^{1/2}$.

Table 6.6 lists the derived densities in a number of planetary nebulae. They range from $n(e^-) \sim 10^2 - 10^6$ cm^{-3}, and are somewhat higher than those found in diffuse nebulae. These densities can then be used with Eqs. (6.41) or (6.42) to make a first order correction to the temperature determination.

So far, we have discussed only lines at visible wavelengths as possible indicators of T or $n(e^-)$. In recent years, sensitive far-infrared detectors have been developed and used to observe fine-structure lines from airborne and balloon-borne telescopes that can be flown above the bulk of the Earth's atmosphere. For example, the [O III] $^3\text{P}_0 - ^3\text{P}_1$ line lies at 88 μm and the $^3\text{P}_1 - ^3\text{P}_2$ line at 52 μm. These far-infrared lines have much smaller excitation energies than the optical lines, such as the $^1\text{D}_2 - ^3\text{P}_2$ transition at 5007 Å. Thus, the ratio $I_{5007}/I_{52\mu m}$ depends strongly on temperature, but, since the $^3\text{P}_2$ level has a much lower critical electron density than $^1\text{D}_2$ does, the ratio also depends on density. On the other hand, the ratio $I_{52\mu m}/I_{88\mu m}$ hardly depends on temperature (since both excitation energies are so low in comparison with typical nebular temperatures), but does depend

Table 6.6 – Electron Densities in Planetary Nebulae

Nebula	[O II]		[S II]	
	$\dfrac{\lambda 3729}{\lambda 3726}$	N_e [a] (cm^{-3})	$\dfrac{\lambda 6716}{\lambda 6731}$	N_e [a] (cm^{-3})
NGC 40	0.78	1.1×10^3	0.69	2.1×10^3
NGC 650/1	1.23	2.1×10^2	1.08	4.0×10^2
NGC 2392	0.78	1.1×10^3	0.88	9.1×10^2
NGC 2440	0.64	1.9×10^3	0.62	3.2×10^3
NGC 3242	0.62	2.2×10^3	0.64	2.8×10^3
NGC 3587	1.30	1.4×10^2	1.25	1.8×10^2
NGC 6210	0.47	5.8×10^3	0.66	2.5×10^3
NGC 6543	0.44	7.9×10^3	0.54	5.9×10^3
NGC 6572	0.38	2.1×10^4	0.51	8.9×10^3
NGC 6720	1.04	4.7×10^2	1.14	3.2×10^2
NGC 6803	0.57	2.8×10^3	–	–
NGC 6853	1.16	2.9×10^2	–	–
NGC 7009	0.50	4.6×10^3	0.61	3.3×10^3
NGC 7027	0.48	5.2×10^3	0.59	4.0×10^3
NGC 7293	1.32	1.3×10^2	1.28	1.6×10^2
NGC 7662	0.56	3.0×10^3	0.64	2.8×10^3
IC 418	0.37	3.2×10^5	0.49	9.5×10^3
IC 2149	0.56	3.0×10^3	0.57	4.6×10^3
IC 4593	0.63	2.0×10^3	–	–
IC 4997	0.34	1.0×10^6	0.45	1.0×10^5

[a] N_e given for assumed $T = 10^4$ ° K; for any other T divide listed value by $(T/10^4)^{1/2}$.

strongly on density. Thus, by measuring these two [O III] ratios, we can determine both T and $n(e^-)$ from observations of a single species, as Figure 6.10 illustrates.

The main problem of this technique is that the beamsize of the far-infrared measurements is often larger than that of the optical observations (remember diffraction!), so that the same area is not always measured in both spectral regions.

(vi) Abundance Determinations

Once T and $n(e^-)$ have been determined, abundances can be inferred from the measured intensities according to Eq. (6.32), together with a model of the structure of the nebula. In the simplest case, the nebula is assumed to be homogeneous with constant T and $n(e^-)$. More sophisticated schemes take the spatial variation of temperature and density into account, and try to develop a complete model of a nebula which reproduces all of the observed properties. Note that often only one or two stages of ionization of an element can be observed, such as O^+ and O^{++}, and that corrections for the unobserved stages of ionization have to be applied to derive the total oxygen abundance.

In general, the derived abundances of the various elements in nebulae agree well (within factors of 2-3) with the solar abundances listed in Table 6.3.
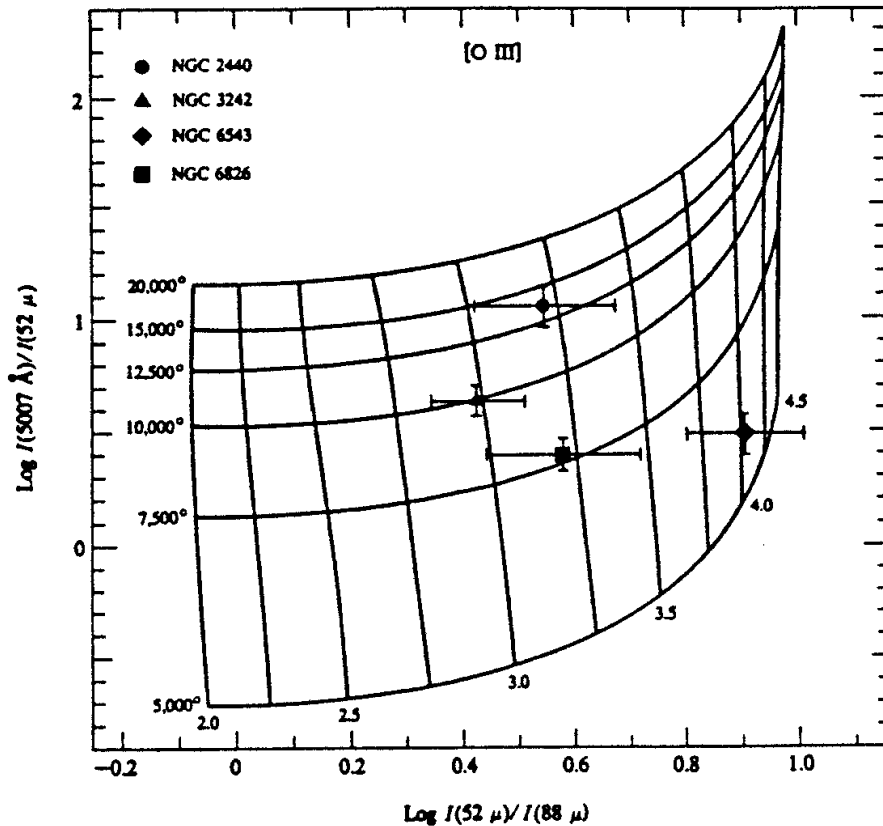
Figure 6.10– Calculated variation of [O III] forbidden-line relative intensity ratios as a function of T(5000 to 20000 K) and $n(e^-)$. Observed planetary ratios are plotted with an indication of probably errors.

(vii) X-Ray Nebulae

In some regions, such as e.g. supernova remnants (SNR), T Tauri stars, or active galactic nuclei, the gas can be subjected to intense X-rays. The cross sections for absorption of X-rays are small, so that the X-rays penetrate substantial column depths of hydrogen. In contrast with the case of the diffuse and planetary nebulae, the transition zone between H^+ and H is therefore not sharp, but consists of a quite extensive region of partly ionized and partly neutral material. Figure 6.11 shows this distribution for a particular model of a gas irradiated by an X-ray source. In such nebulae, Auger processes are an important source of highly-stripped ions and charge-transfer is an important neutralizing process. The competition between these two processes can be seen in Figure 6.11, since the peak in the Si IV distribution lies beyond (i.e., farther from the ionization source) the Si III peak. Why? Following K-shell ionization of Si II, Auger ionization produces Si IV, which, as the neutral hydrogen fraction increases, is replaced by Si II as the major ionization stage.

Because the charge-transfer rates for Ne^{2+} and S^{2+} with H are extremely slow, Ne III and S III persist well into the neutral region. The ionization structure of a plasma in the region where X-rays are significant may be modified by collisional ionization processes, which will be discussed in the next section.
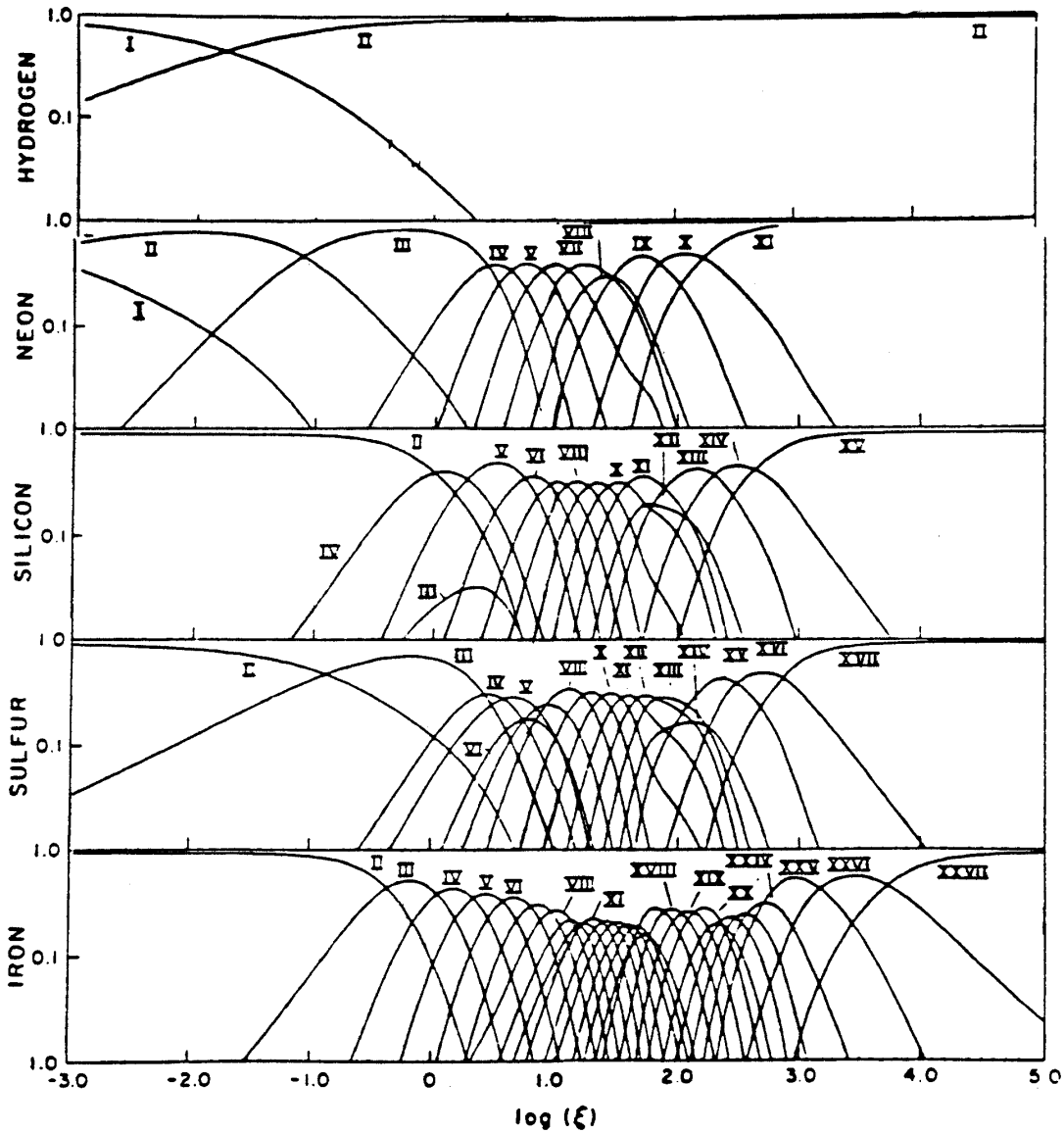
Figure 6.11– The ionization distribution for an optically thin gas illuminated by an X-ray source (at right). The parameter ξ is proportional to the ionizing flux F_ν.

(b) Collisionally-Ionized Regions of the ISM

(i) Hot Coronal Gas

Ultraviolet absorption line studies with the spectrometer aboard the Copernicus satellite have revealed the presence of highly ionized material throughout the interstellar medium. In particular, the $1s^2 2s$ ^{2}S – $1s^2 2p$ ^{2}P O VI lines at 1032 and 1038 Å were discovered in nearly all directions, and suggest a global distribution of O^{5+} (Jenkins & Meloy 1974, *Ap. J.* **193**, L121).

Although hot stars or X-ray sources can produce such high stages of ionization locally by photoionization, they cannot maintain it throughout the ISM. Such highly ionized

material can be produced in a hot gas (T$\sim 10^6$ K) via electron collisions such as

$$e^- \; + \; X^{m+} \quad \rightarrow \quad e^- \; + \; X^{(m+1)+} \; + \; e^- \tag{6.45}$$
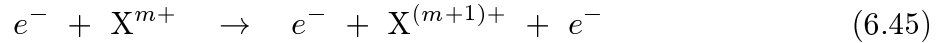
that produce the ionization. The recombination of the gas occurs, as for the case of a photoionized nebula, by dielectronic and radiative recombination.

Because the electrons control both the ionization *and* the recombination in this case, the equilibrium distribution of ionization stages is independent of the electron density at low densities, and is a function only of the temperature. Such an equilibrium is called a *coronal equilibrium*, because it characterizes the conditions in the solar corona (see §VI.3).

The computed ion distributions for carbon, nitrogen, and oxygen are illustrated in Figures 6.12a-c for a range of temperatures. The distributions reflect the magnitudes of the ionization potentials, which enter the collisional ionization rates. The temperature at which one ionization stage X^{m+} is replaced by the succeeding stage $X^{(m+1)+}$ is usually at $kT\sim$0.2-0.3 $I(X^{m+})$, so that the existence of a particular ionization stage provides a good indication of the temperature of the hot gas. Thus, the presence of O^{5+} in the ISM suggests a temperature near 3×10^5 K.

Evidence for the presence of hot gas throughout the ISM also comes from observations of continuum X-ray emission produced by radiative recombination, two-photon decay of hydrogen- and helium-like ions, and bremsstrahlung. Superposed on this continuum are spectral lines from levels populated by recombination, electron-impact excitation, or inner shell ionization. Figure 6.13 illustrates the X-ray spectrum for a low density plasma at 10^6 K. Most of the emission is electric dipole in nature, such as the n = 2 $\rightarrow$ 1 resonance transitions of H- and He-like ions of the abundant elements Ne, O, N, and C.

(ii) Galactic Halo

Absorption lines of Si^{3+}, C^{3+}, and N^{4+} toward distant stars show that the galaxy has an extended halo with highly-ionized species. If these ions are produced in a hot gas by collisional ionization, its temperature would be between 6×10^4 and 2×10^5 K.

An alternative explanation of these highly-excited species in the galactic halo involves photoionization by hot white dwarfs, galactic X-ray sources, and the extragalactic X-ray background. See Savage, *Spectroscopy of Astrophysical Plasmas*, Ch. 8, for further details.

(iii) Nova and Supernova Remnants

Many recent novae are surrounded by small, faint shells with emission line spectra. These are usually tiny, *photoionized* nebulae. A few emission nebulae are known to be supernova remnants, of which the Crab nebula, the remnant of the supernova A.D. 1054, is the best known example. In this case, the radiation source has a very **non**-thermal spectrum (i.e., it cannot be fitted by a blackbody), but has the shape

$$L_\nu \quad = \quad c\nu^{-n} \tag{6.46}$$

with n of order unity. Thus, it has a strong component at ultraviolet and X-ray wavelengths, which can result in substantial **photo**ionization of the gas. However, in other supernova remnants, no photon source is seen, so that collisional ionization must dominate their spectra.

In Figure 6.14a, the X-ray spectrum of the Puppis A supernova remnant is shown. The inferred temperature in this case is about 3×10^6 K, hot enough to *collisionally* ionize most species. The Lyman α 2p – 1s and Lyman β 3p – 1s lines of N^{6+}, O^{7+}, and Ne^{9+} are prominent features, as are lines of the helium-like ions O^{6+} and Ne^{8+}. Unfortunately, the spectral resolution of these observations was too low to show the satellite lines resulting from the dielectronic recombination.

Note that both for photoionized nova shells, and collisionally ionized supernova remnants, the recombination time is long compared with the expansion time, and that no further ionizations take place after the initial ionization. Thus, the ionization is "frozen in" while the gas cools down considerably. This leads to spectra in which recombination lines of various species can be very prominent, whereas the temperature of the gas is quite low. For example, Figure 6.14b shows the spectrum of the CP Pup nova shell, which has an estimated temperature of T~800 K. This shell has a very high nitrogen abundance, which results in prominent recombination lines of the various ionization stages of nitrogen.
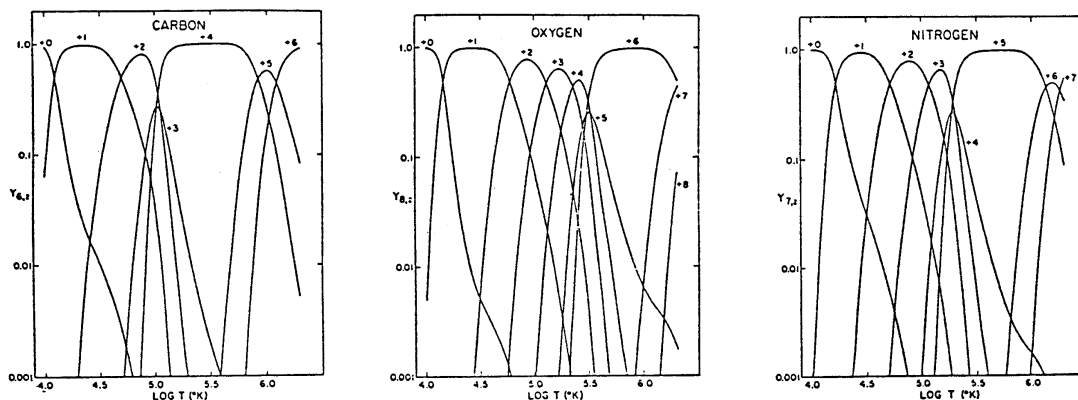
Figure 6.12– Computed ion distributions for C, O, and N for a range of temperatures.
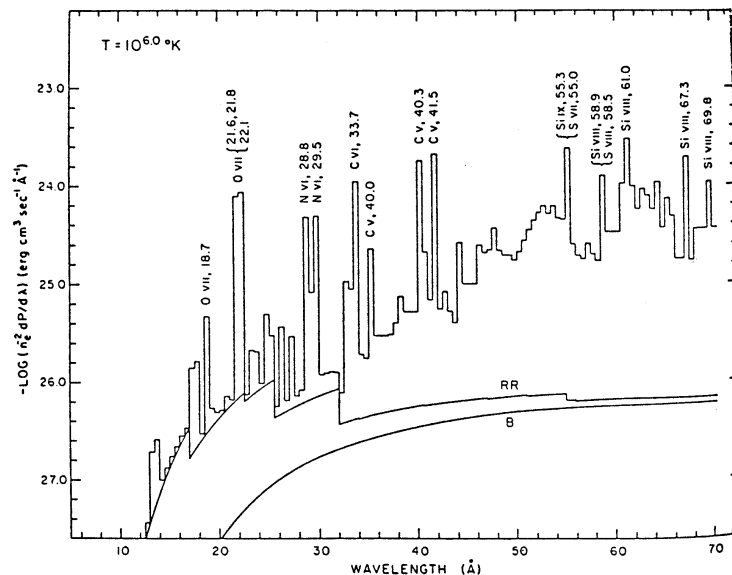
Figure 6.13– X-ray spectra of a low density plasma, with T~10^6 K. Steady-state ionization equilibrium (SS) at 10^6 K is assumed, using "cosmic abundances."
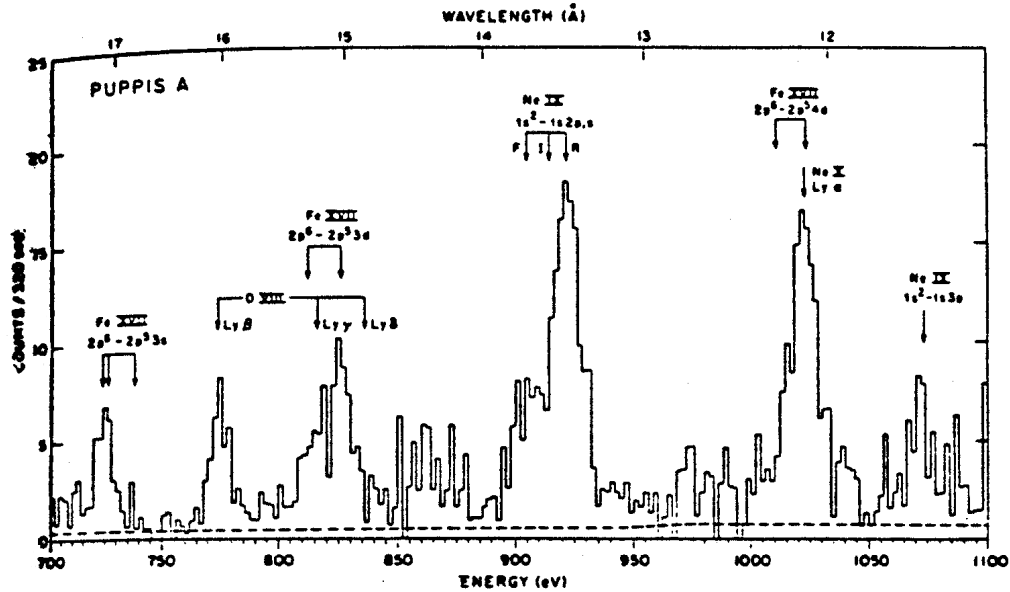
Figure 6.14a– X-ray spectrum (700-1100 eV) of the Puppis A supernova remnant as observed by the Einstein FPCS. Data from 14 scans with the TAP crystal are combined. The dashed line indicates the background level.
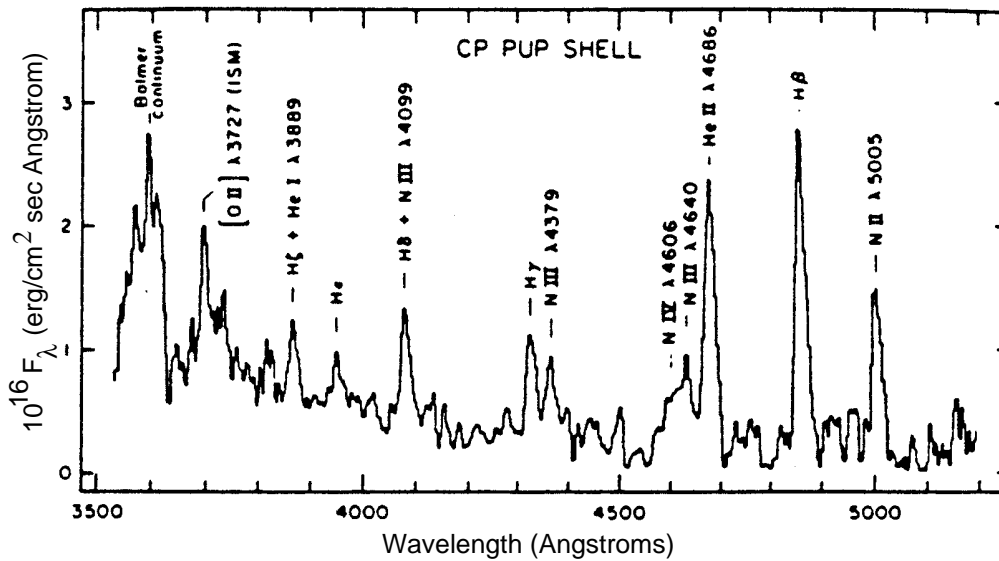
Figure 6.14b–Optical spectrum of a recombining cool (T∼800 K) nova plasma.

3. The Solar Corona

As another example of a hot dilute gas, we consider the solar corona. Because it is so close, it can be studied in detail and is typical of the outer atmospheres of many stars, which show strong emission at X-ray wavelengths. For a good review of the spectroscopy of the solar corona, see Zirker in *Spectroscopy of Astrophysical Plasmas*, Ch. 6. This section is based largely on this review.

Figure 6.15 shows a schematic diagram of the sun, whereas Figure 6.16 outlines the appropriate temperature and density variation with height in the region of the solar
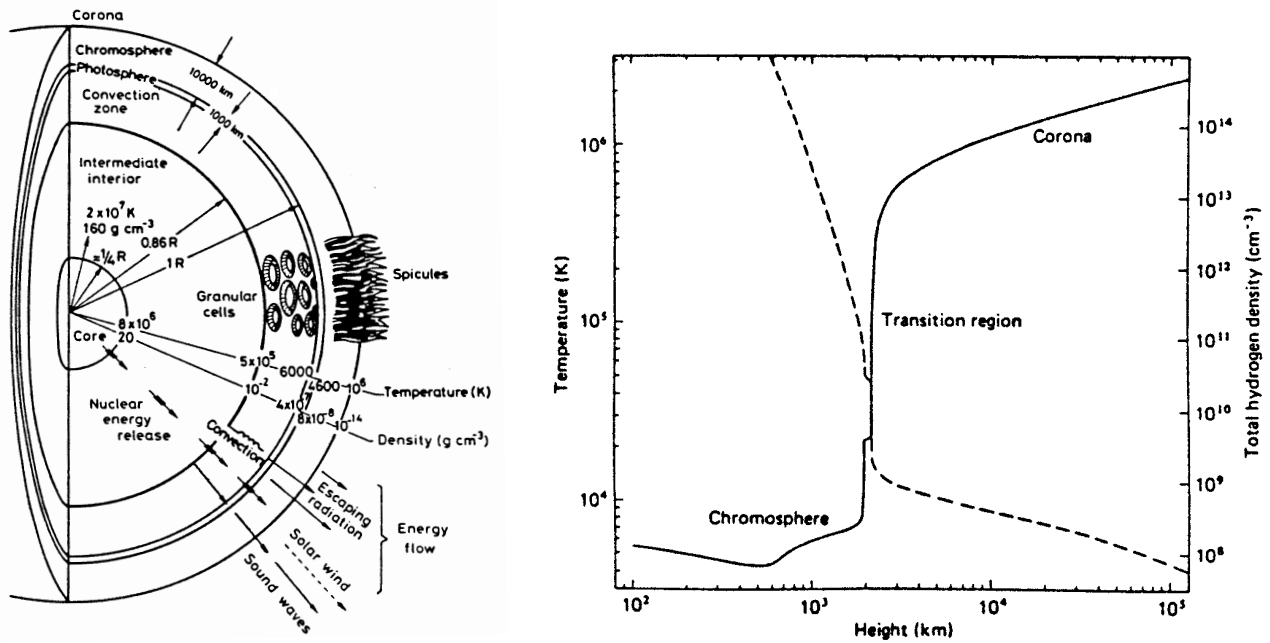
Figure 6.15– (Left) A schematic cross section of the Sun. **Figure 6.16a**– (Right) Variation with height of the temperature and density in a one-dimensional model of the solar atmosphere. $h = 0$ occurs where $\tau=1$ at 500 nm (*ARAA* **15**, 363 (1977)).
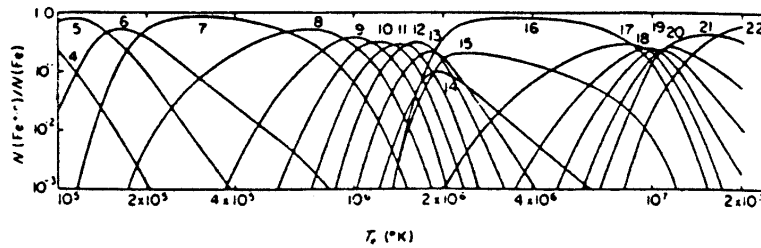
Figure 6.16b– The temperature variation of the ionization equilibrium of iron, under coronal conditions. The figures on the curves correspond to the number of missing electrons.

chromosphere and the corona. The first coronal emission line, $\lambda5303$ Å, was discovered during the total solar eclipse in 1869, and by 1927 nearly 16 lines were known. However, it was not until the end of the 1930's that it was realized that they belong to highly-ionized atoms. For example, the famous "red coronal" line at $\lambda6374$ Å was shown by Grotian in 1939 to be due to the ground state fine-structure transition of Fe X: $3p^5\ ^2P_{3/2} - {}^2P_{1/2}$.

Once most of these lines were identified, it became clear that (i) the gas is very hot, $T\sim10^6$ K, and (ii) it is dilute, because the lines are strong, so collisional de-excitations are still rare. At such high temperatures, the ionization is again caused by collisional processes. However, the corona is not in thermodynamic equilibrium, so it does not have a single, well-defined temperature. The fundamental temperature, as in the case of nebulae, is therefore the kinetic temperature of the ions or electrons. The ionization structure can again be computed from the equilibrium of the collisional ionization and recombination processes. Figure 6.16a shows the resulting structure for iron as a function of temperature. A given ion, such as e.g. Fe^{9+}, is abundant over only a relatively narrow temperature
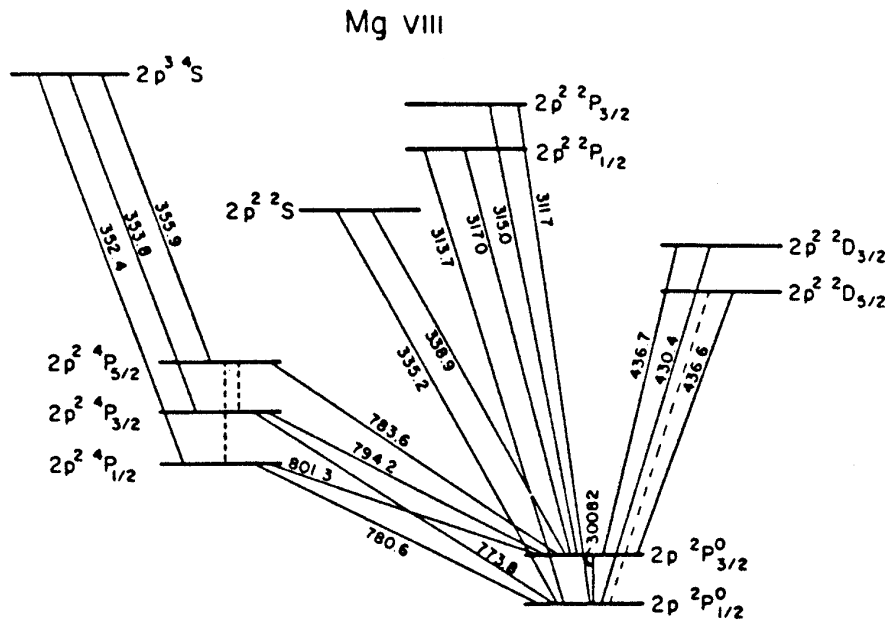
Figure 6.17– Energy level diagram for Mg VIII, showing the transitions used to determine the coronal density.
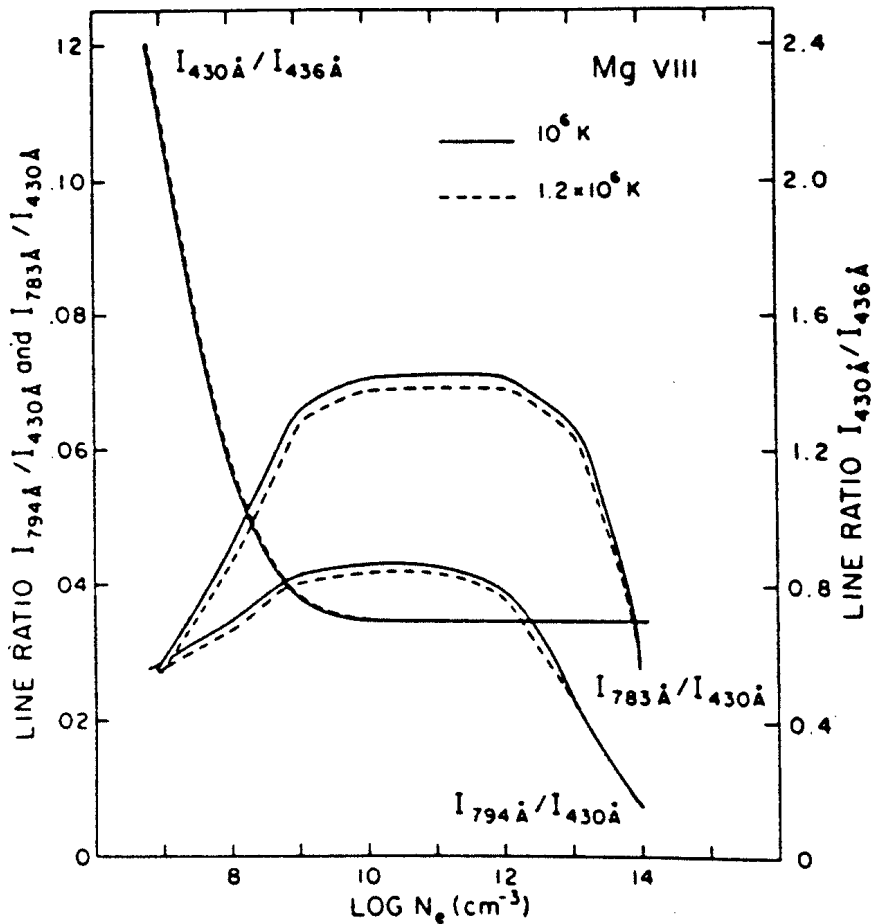
Figure 6.18– The calculated population ratio $^4P/^2P$ as a function of electron density.

range. Thus, the presence of Fe X lines in the coronal spectrum immediately signifies the presence of a layer with a narrow temperature range. The strength of the line is then a measure of the electron density in the region.

As we have seen for nebulae, there are other, more accurate ways to measure temperature and density, namely through observations of *ratios* of lines. For example, extreme ultraviolet lines of the Mg^{7+} ion have been used to determine the electron density in the transition zone between the chromosphere and the corona. Figure 6.17 illustrates the energy levels involved. At low densities, nearly all Mg^{7+} ions will be in the ground 2p ^2P state, but at high densities, the metastable ^4P level will be significantly populated, and a Boltzmann distribution between the levels will be established (c.f. Eq. 6.25). Thus, the population ratio $^4P/^2P$, or equivalently, the ratio of the intensity of the resonance line ^2D - ^2P at 430 Å and the intercombination line ^4P - ^2P at 783 Å, is a measure of the electron density. Figure 6.18 shows the computed line ratio as a function of electron density. A similar analysis can be carried out for chromospheric and coronal lines.

Because each ion exists only over a narrow temperature range, each spectroscopic diagnostic is useful only over a relatively limited range of T or $n(e^-)$. Special diagnostics have therefore been developed for the extreme conditions encountered in solar flares, in which the electron temperatures may exceed 10^7 K. At such high temperatures, elements such as Ne, O, Mg, and Ca become helium-like, i.e., stripped down to two electrons. Consider as an example the case of O VII, for which the energy levels are illustrated in Figure 6.19.
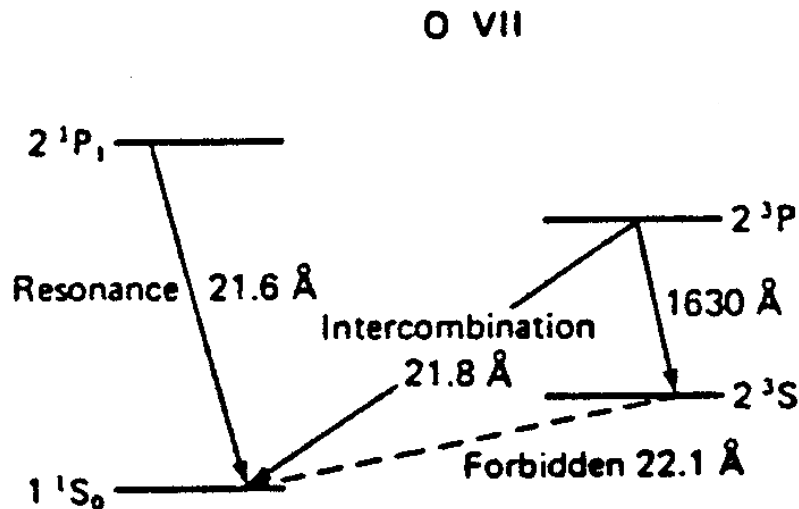
Figure 6.19– Energy level diagram for O VII.

At "low" electron densities $(n(e^-) \lesssim 10^9$ cm$^{-3})$, the metastable 2 ^3S level decays radiatively under emission of the forbidden 22.1 Å line. The 2 ^3P level is populated by collisions from the ground state, and also decays radiatively in the intercombination line at 21.8 Å. In this regime, the intensity ratio 22.1/21.8 Å > 1. However, at higher densities, $n(e^-) \gtrsim 10^{10}$ cm^{-3}, collisional processes can excite the 2 ^3S effectively to the 2 ^3P level. As a result, the 2 ^3P population increases relative to 2 ^3S, so that the line ratio

$\lambda 22.1/\lambda 21.8$ decreases to less than unity. Using this method, values of $n(e^-) \sim 10^{11}$ - 10^{12} cm^{-3} have been derived for flares.

Satellite lines due to recombination of lithium-like ions have been observed as well in the solar corona. The intensity ratio of these lines with respect to the resonance lines of the helium-like ions can be used as a measure of the electron temperature. Figure 6.20 illustrates the general level scheme involved.
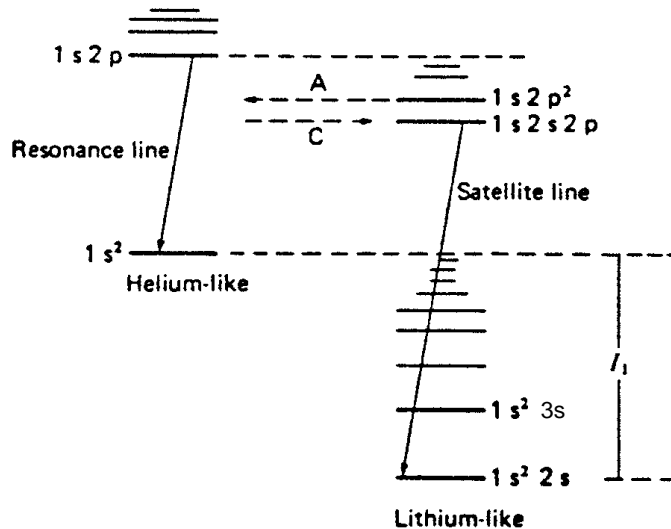

Figure 6.20– A term diagram for a lithium-like ion and its associated helium-like ion, illustrating the origin of satellite lines.

4. Active Galactic Nuclei

a) Optical Spectroscopy

Many galaxies in addition to having their own H II regions and planetary nebulae, show in their spectra of their nuclei characteristic nebular emission lines. In most of these objects, the gas is most likely photoionized by hot stars in the nucleus, so that the region can be thought of as a giant H II region, or even a cluster of many H II regions. The galactic nuclei with the strongest emission lines of this type are often called "starburst galaxies." Figure 6.21 shows a typical spectrum.

Besides these objects, a small fraction off (spiral) galaxies have ionized gas that emits a line spectrum with a *wider range* of ionization than any H II region. These galaxies are called *Seyfert* galaxies. Quasars (quasi-stellar radio sources) and QSOs (quasi-stellar objects) show similar spectra, but they are much rarer in space. Together, these objects are called *active galactic nuclei* (AGN). A detailed discussion of their spectra is given in Ch. 11-12 of *Astrophysics of Gaseous Nebulae and Active Galactic Nuclei*, and also in Ch. 3 of *Spectroscopy of Astrophysical Plasmas*, both by Osterbrock. Here we summarize a few of their characteristics.

The Seyfert galaxies can be classified on the basis of their spectra into two main types, Seyfert 1 and 2, with further subdivisions possible. Seyfert 1 galaxies have very broad H I, He I, and He II lines with widths ranging from 5000-30000 km/s, while the forbidden

lines are narrower with widths of about 500 km/s. An example is shown in Figure 6.22. Note that even broad permitted lines of Fe II appear. Such Fe II lines are not observed in planetary nebulae or diffuse nebulae, but they are seen in, for example, the spectra of T Tauri stars. In Seyfert 2 galaxies, on the other hand, both the permitted and forbidden lines have the same width, about 500 km/s, as the example in Figure 6.23 shows. The spectrum of an intermediate-type Seyfert 1.5 galaxy was shown in the Introduction, it has both narrow and broad H I profiles.

What mechanism produces these ions and lines?

(i) Narrow Line Region

The narrow lines in the spectra of AGN are similar to those of an H II region or planetary nebula, except that the range of ionization is greater. This indicates a low density, ionized gas with more or less normal abundances. Using, e.g., the [O III] ($\lambda 4959$ + $\lambda 5007$)/$\lambda 4363$ ratio discussed earlier as an indicator of temperature, T$\sim$10,000-20,000 K is found. This is a strong indication that the main energy input is by *photoionization*. If the gas were collisionally ionized, T$>$30,000 K would be expected for the region in which [O III] is dominant. The best observable density indicator is the [S II] $\lambda 6717/\lambda 6731$ ratio, which suggests $n(e^-) \sim 10^{3.5\pm1}$ cm^{-3} in many objects.

In order to produce the wide range of ionizations observed in Seyfert galaxies, a "hard" spectrum is required extending far into the ultraviolet. The high energy photons ($h\nu >$100 eV) of such a hard spectrum will then produce the observed highly ionized species such as Ne^{4+} and Fe^{6+} near the central source, and they will also produce a long, partly ionized transition zone in which H, H$^+$, O, O$^+$, and S$^+$ coexist. Thus, the situation is very similar to that of X-ray nebulae. For Seyfert galaxies, the spectrum is typically

$$ L_\nu \quad = \quad c\nu^{-\alpha} \qquad , \tag{6.47} $$

with $\alpha \sim$1-2.

(ii) Broad Line Region

The physical situation in the broad line region is considerably different. One characteristic of this region is that all the observed lines are electric dipole allowed, whereas none of the forbidden lines have similar broad profiles. This must mean that the gas density in the broad line region is so high that all the levels of the abundant ions that give rise to the forbidden lines are collisionally de-excited, i.e. $n(e^-) >> n_{cr}$ for the forbidden lines, so that they are relatively weak. This implies $n(e^-) \gtrsim 10^8$ cm^{-3}. Observations of the C III $\lambda 1909$ intercombination line suggest $n(e^-) \sim 10^9$ cm^{-3}.

There is little direct information on the temperature since the H and He lines provide no direct diagnostics. The presence of the Fe II lines suggests that the temperature cannot be too high, T$\lesssim$ 40,000 K, because otherwise it would be ionized to Fe III, etc.

The energy input from the central source to the broad line region is not so clear as in the case of the narrow line region. Most likely, it is still photoionization, as in the narrow line region. The large widths of the lines result from Doppler shifts due to mass motions, but the cause for these motions is still not definitively established, and is one of the major problems in the study of AGN.
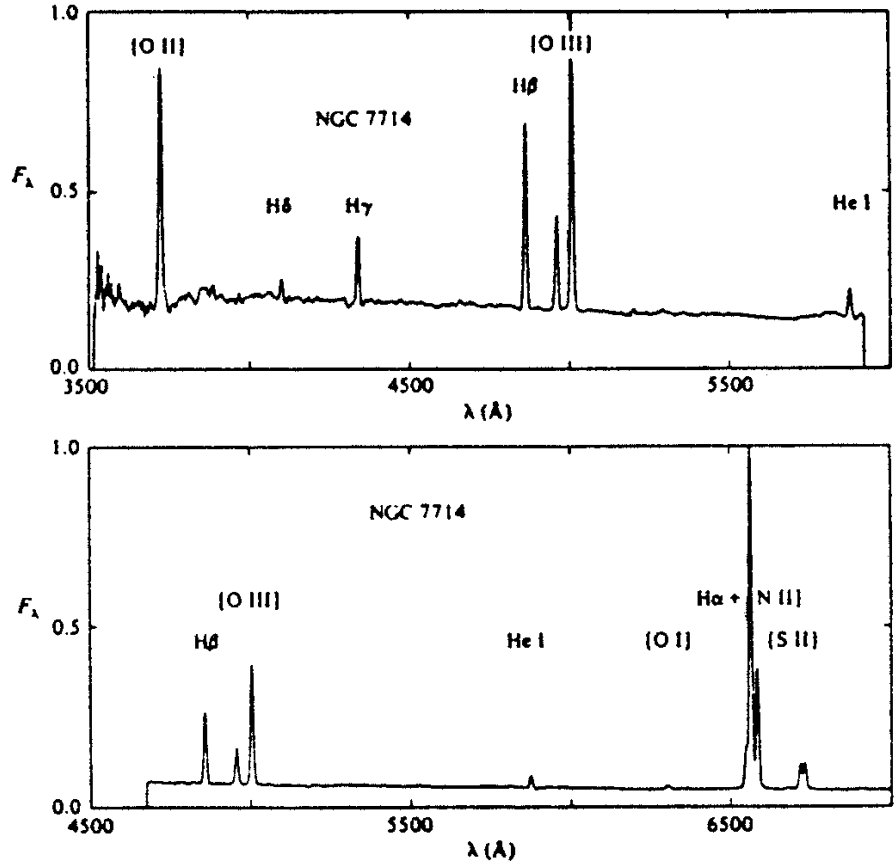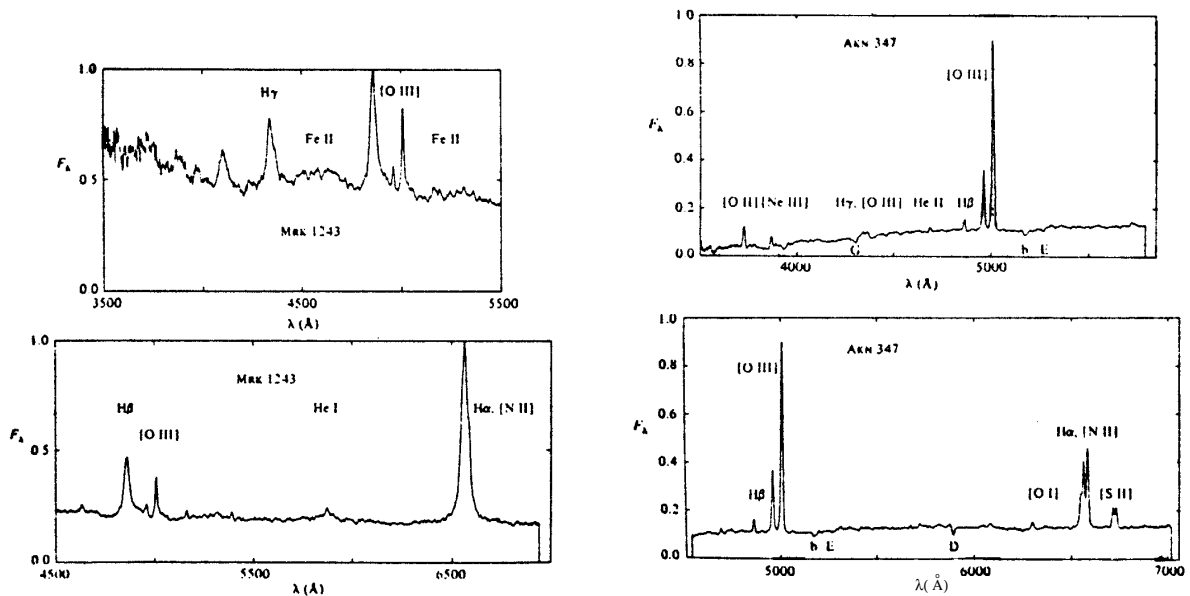
Figure 6.21– NGC7714, a narrow-emission-line or "starburst" galaxy.

Figures 6.22 (left) and 6.23(right)– MRK 1243 and AKN 347, Seyfert 1 and Seyfert 2 galaxies, respectively.
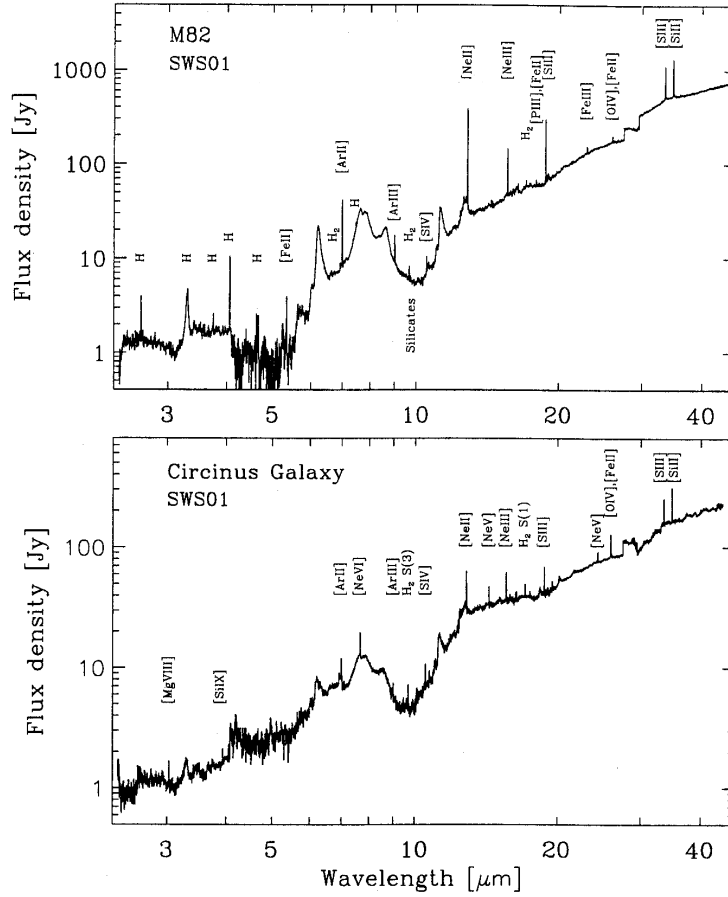
Figure 6.24– Full 2.5-45 μm ISO SWS spectra of the starburst galaxy M82 (upper panel) and the Seyfert 2/starburst galaxy Circunis.

b) IR Spectroscopy of AGN/ULIRGs

A key discovery of the IRAS satellite was the detection of very luminous ($L \geq 10^{11-12}L_\odot$) galaxies, where the SED is such that most of the radiation is emitted at mid- to far-infrared wavelengths. Optically, these galaxies often resemble the narrow line AGN described above. These so called ULIRGs (UltraLuminous InfraRed Galaxies) are very gas and dust rich, with gas masses inside the central 1 kpc of order $\sim10^{10}$ $M_\odot$. They are often members of interacting, or merging, galaxy groups. Thanks to the ongoing development of improved IR detectors, and with the launch of the Infrared Space Observatory (ISO) above the highly absorbing Earth's atmosphere (about which we'll have much more to say later), mid-infrared spectroscopy of these objects became possible for the first time.

Important atomic lines at these wavelengths include the fine structure emission of a variety of ionized atoms. As in galactic HII regions, photoionization in AGN and ULIRGs creates the observed emission. The key question is whether the photons are produced by a burst of star formation or by a central AGN (read: black hole). High spatial resolution observations are one way to go, spectroscopy is another. Figure 6.24 present the ISO

– 136 –

Short Wavelength Spectrometer (ISO SWS) spectrum of two galaxies, namely M82 and Circunis, which are clearly quite different. In M82, the spectrum is dominated by reasonbly low ionization potential species such as NeII, SIII, SiII, and ArII; in Circunis we see these along with rather intense fine structure emission lines from atoms with ionization potentials up to 320 eV (OIV, NeV, NeVI, MgVIII, SiIX; we'll learn about the silicate features at 10 μm and the so-called PAH emission from 7-12 μm later in the class), including several "coronal" lines analogous to those discussed above! For those interested in more details, see Moorwood et al. 1996, *Astron. Ap.* **315**, L109; and Oliva et al. 1994, *Astron. Ap.* **288**, 457. Clearly, the M82 spectrum can easily be accounted for by an appropriate number of HII regions, while the spectrum of Circunis, with its mix of low and high ionization potential species, can only be generated with a source of very hard UV and X-ray photons near the nucleus. Such fine structure lines are much more numerous in the IR than in the optical, and so IR spectroscopy thus forms an excellent diagnostic of starbust versus AGN activity in nearby galaxies.

5. Atomic Spectroscopy & the High Redshift Universe

Telescopes are time machines. As we look to increasingly greater distances with new and more powerful instruments, we look further back in time. One way to characterize the look back time is via the **redshift**, which is defined such that the observed wavelength of a spectral line (say the Hα line of atomic hydrogen) in a distant object is given by $\lambda_{obs} = (1 + z)\lambda_{rest}$, where λ_{rest} is the rest wavelength of the line. The redshift can be used either as a measure of distance from us, or the time since the creation of the universe. The present epoch is at $z = 0$, corresponding to a time some $t \sim 2 \times 10^{10}$ years after the Big Bang.

Our knowledge about the high redshift universe ($z > 1$) has increased tremendously in just the last few years as better instruments and, just as importantly, better means of finding high redshift galaxies have become available. One of the most successful methods for imaging high redshift galaxies involves the so-called Lyman break technique, shown graphically for galaxies at $z \sim 3$ in Figure 6.25.

By carefully selecting broadband filters that lie to the red and blue of the Lyman continuum break, this technique enables the distant universe to be efficiently surveyd using the "colors" of the objects imaged in the three distinct bands. High redshift galaxies are distinctly red in this classification scheme, and recent surveys have some 1500 candidate objects within them. In order to study their properties in additional detail, it is essential to know their distance. Two major methods have emerged to date.

When optical spectra of high redshift galaxies are acquired, it is the rest frame *ultraviolet* region that is probed. Figure 6.26 presents one such example, for the $z = 2.729$ galaxy MS 1512-cB58. In this case, gravitational lensing by a foreground cluster increases the apparent luminosity of this galaxy by a factor of 30, and so it is one of the few high redshift galaxies for which its interstellar medium has been characterized in such detail. Overall, the UV properties of MS 1512-cB58 are similar to those of nearby star-forming galaxies. From the observed interstellar absoprtion lines, the deduced metallicity (unfortunately labeled with a capital Z) is $Z_{cB58} \approx 1/4 \; Z_\odot$. This metallicity is very large considering the age of such objects, and is a factor of a few larger than that of "typical" Lyman break galaxies near this redshift.
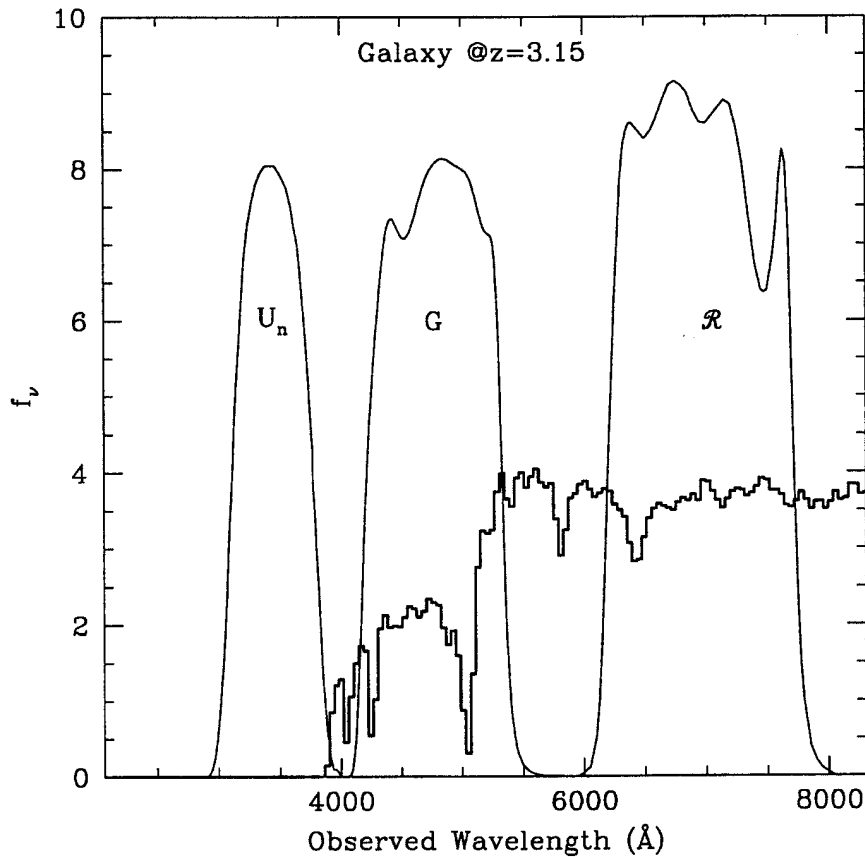
Figure 6.25– An illustration of how photometric imaging systems can be "fine tuned" for observing the Lyman continuum break at a redshift of $z \sim 3$. In addition to the passbands of the filters used, the plot presents a model galaxy spectrum that includes both an ensemble of stars and netrual hydrogen gas, including gas inbetween the galaxy and observer over a range of redshifts. This Lyman α forest is reponsible for the absorption blueward of the galaxy's Ly α transition at 5050 Å.

Figure 6.27 presents the near-infrared spectrum of this same galaxy, which now corresponds to a rest frame *optical* spectrum like those presented for the Seyfert galaxies above. Such observations are assuming increasing importance because the effects of obscuration of dust become extremely important at short wavelengths. There is in fact a class of objects, called "extremely red objects" or EROs, that cannot be observed even with the largest ground based telescopes at optical wavelengths. For MS 1512-cB58, the redshift deduced from the near-IR observations is $z = 2.723$, systematically to the blue of that derived in the rest frame UV. The derived oxygen abundance is 1/3rd solar, in good agreements with that derived from the optical spectrum. Together, these observations support the existance of large-scale outflows in the interstellar medium of such galaxies, galaxies that are forming stars at a prodigious rate. The role of such winds in enhancing the metallicity of the interstellar gas in such galaxies and in allowing the escape of ionizing photons to the intergalactic medium is currently a subject of considerable research.
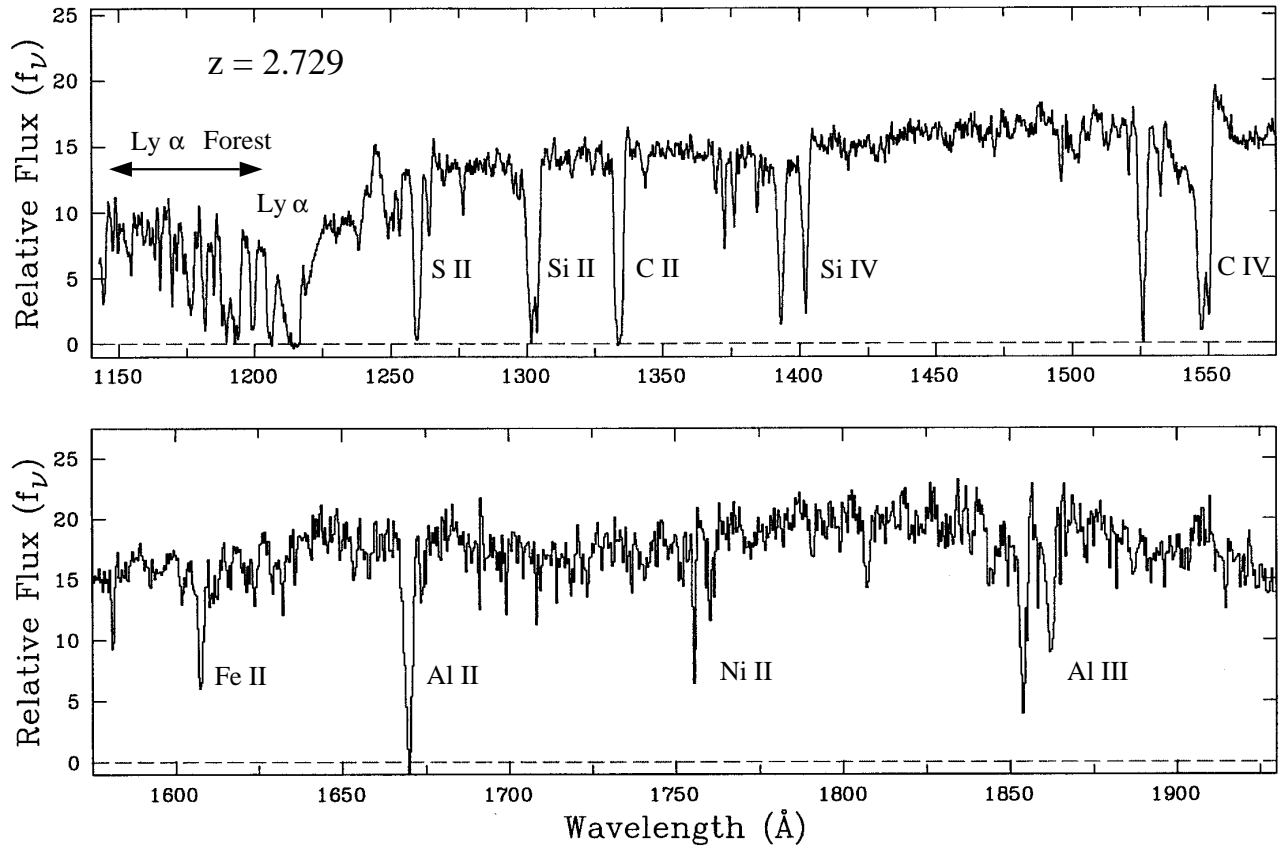
Figure 6.26– Rest frame UV spectroscopy of the high z galaxy MS 1512-cB58, obtained with the Keck LRIS spectrometer. Strong interstellar absorption lines are identified, in addition to Ly α (which is highly optically thick). The Lyman α forest is caused by "H I cloudlets" lying at a range of redshifts between MS 1512-cB58 and the earth.
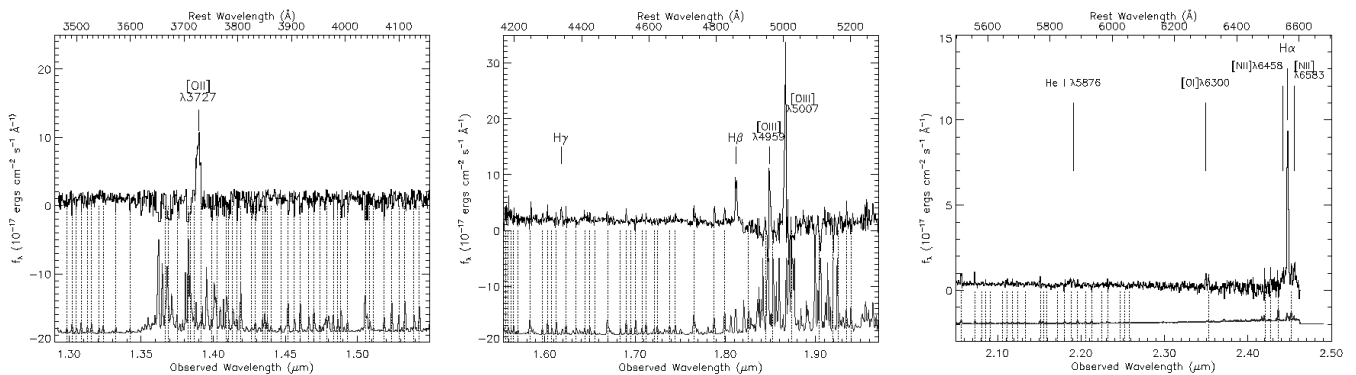

Figure 6.27– Rest frame optical spectroscopy of the high redshift galaxy MS 1512-cB58, obtained with the Keck NIRSPEC spectrometer. The heavier plot at bottom depicts the atmospheric emisssion versus wavelength.

6. The Terrestrial Atmosphere

The Earth's atmosphere can be divided into several regions, in which the dominant chemical and physical processes differ: the troposphere, the stratosphere, the mesosphere, and the thermosphere. Figure 6.24 illustrates the temperature profile for the various layers. The atmosphere is gravitationally bound, and, to first order, spherically symmetric. The interaction of the solar radiation field and the principal atmospheric constituents determines the vertical structure, e.g. the radiative properties of O_3 determine the temperature structure in the stratosphere, whereas the photoprocesses of O_2 increase the temperatures in the thermosphere to nearly 1000 K. In the upper atmosphere, photoionization by short wavelength solar radiation (UV and X-rays) can produce ions, resulting in the ionosphere. In fact, both positive and negative ions (cations and anions) are present in the ionosphere resulting in a net neutral charge. The ionosphere is often divided into a number of characteristic layers, labeled D, E, and F. Figure 6.25 illustrates the vertical distribution of electron densities in these layers.
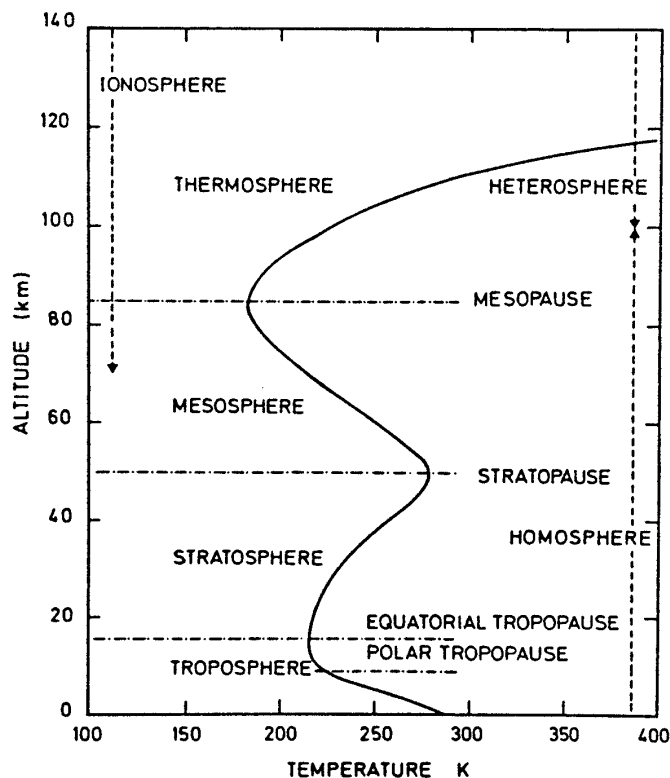
Figure 6.28– Regions of the atmosphere and their thermal structure.

The study of the upper atmosphere of the Earth, and that of the other planets, is called *aeronomy*. It has been defined by Chapman as "the science of that part of the upper atmosphere where dissociation and ionization are important." What we observe from the atmosphere is called the *airglow*, i.e. the amorphous, optical line radiation emitted by planetary atmospheres extending from the far-UV into the near-IR. Note that the term excludes the thermal emission at longer wavelength infrared bands. Historically, airglow was discovered as "the light of the night sky", and later, some very bright emission was also

found in twilight. Experimental techniques for observing airglow emission in full daylight are very difficult.
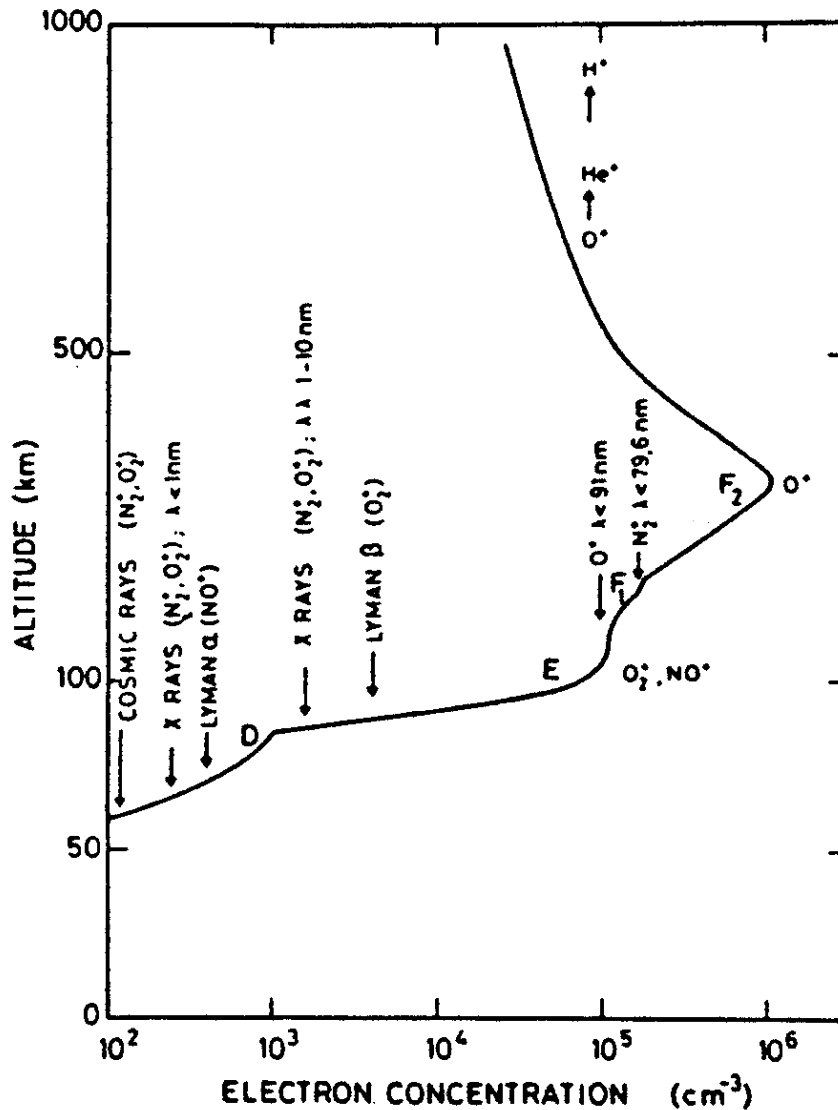

Figure 6.29– Definition of the ionospheric layers based on the distribution of electron density.

The airglow arises from the various atoms and molecules present in the atmosphere, and can be classified into three different categories:

    a) Lines due to direct, resonant scattering of sunlight;

    b) Lines emitted during the creation or destruction of the ionosphere; and

    c) Radiation resulting from the photochemistry of neutral constituents.

Note that low in the atmosphere (the troposphere), the density is so high that collisional de-excitation is very rapid, so that very little emission is seen from that region. Thus, the altitude at which the emission occurs depends in part on the radiative lifetime of the levels involved, and the competition with collisional de-excitation. Figure 6.26 shows the

distribution of the dominant oxygen-bearing species during the daytime in the troposphere and stratosphere. In the troposphere, the densities are greater than 10^{18} cm^{-3}.

The *aurora* also consists of line emission from the upper atmosphere, but it is distinguished from airglow by its excitation source, namely impact of electrons and ions precipitated from outside the atmosphere. It is confined to the magnetic polar and sub-polar regions, and occurs sporadically. The source of the auroral electrons and ions is a large subject of its own, which will not be discussed here. Note that part of the *dayglow* is nearly identical to a faint aurora, except that it is *photo*electrons produced by photoionization during the day that provides the excitation.
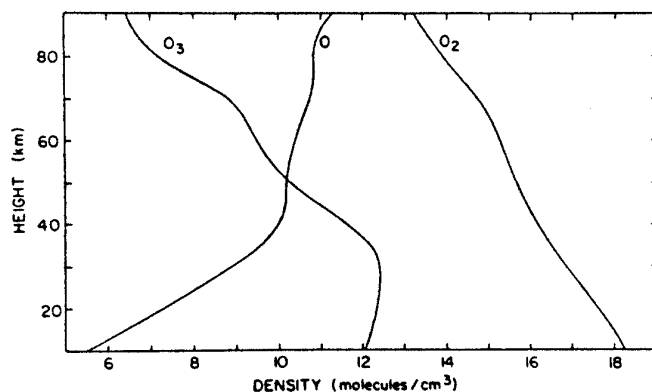
Figure 6.30– Daytime equilibrium of oxygen allotropes according to the Chapman theory.

Many *atomic* species are observed in the Earth's night airglow. The strongest lines are the green ($\lambda5577$ Å ^{1}S – ^{1}D) and red ($\lambda6300$ Å ^{1}D – ^{3}P) forbidden lines of [O I], and the yellow permitted resonance doublet of Na I, 3s ^{2}S$_{1/2}$ – 3p ^{2}P$_{1/2,3/2}$ (c.f. Figure 6.27). The origin of the [O I] lines has been the subject of considerable debate, but it clearly involves molecular processes and will therefore be discussed later – as will a number of other atmospheric applications. In twilight, the Na emission results from *resonance scattering*, i.e., the atom absorbs sunlight in an electric dipole allowed transition, and then radiates rapidly back to the same level. If the emission terminates on a different energy level (e.g. emission from $u \to l_2$, Figure 6.28), the process is called *fluorescence scattering.*

The strength of resonant scattering lines can be expressed in terms of the g-factor (not to be confused with the state degeneracy), also called the photon scattering coefficient, which is defined as

$$g(ul_i) \quad = \quad \pi F_\nu(\infty)\frac{\pi e^2}{m_e c}f_{lu}\frac{\mathrm{A}_{ul_i}}{\sum_j \mathrm{A}_{ul_j}} \quad \text{photons s}^{-1} \quad , \qquad (6.48)$$

where πF_ν is the flux outside the atmosphere in units of photons cm^{-2} s^{-1} Hz^{-1}. Given a specified radiation field, e.g., the solar radiation spectrum at 1 AU (**a**stronomical **u**nit) from the Sun, the g-values can be calculated once and for all for a transition of a given atom. The column density of emitting atoms can then be computed from the measured mean intensity. At night, no sunlight is present to produce resonant scattering, so the Na emission is probably due to chemical reactions between Na and O_3, which eventually leave the Na in an excited state.
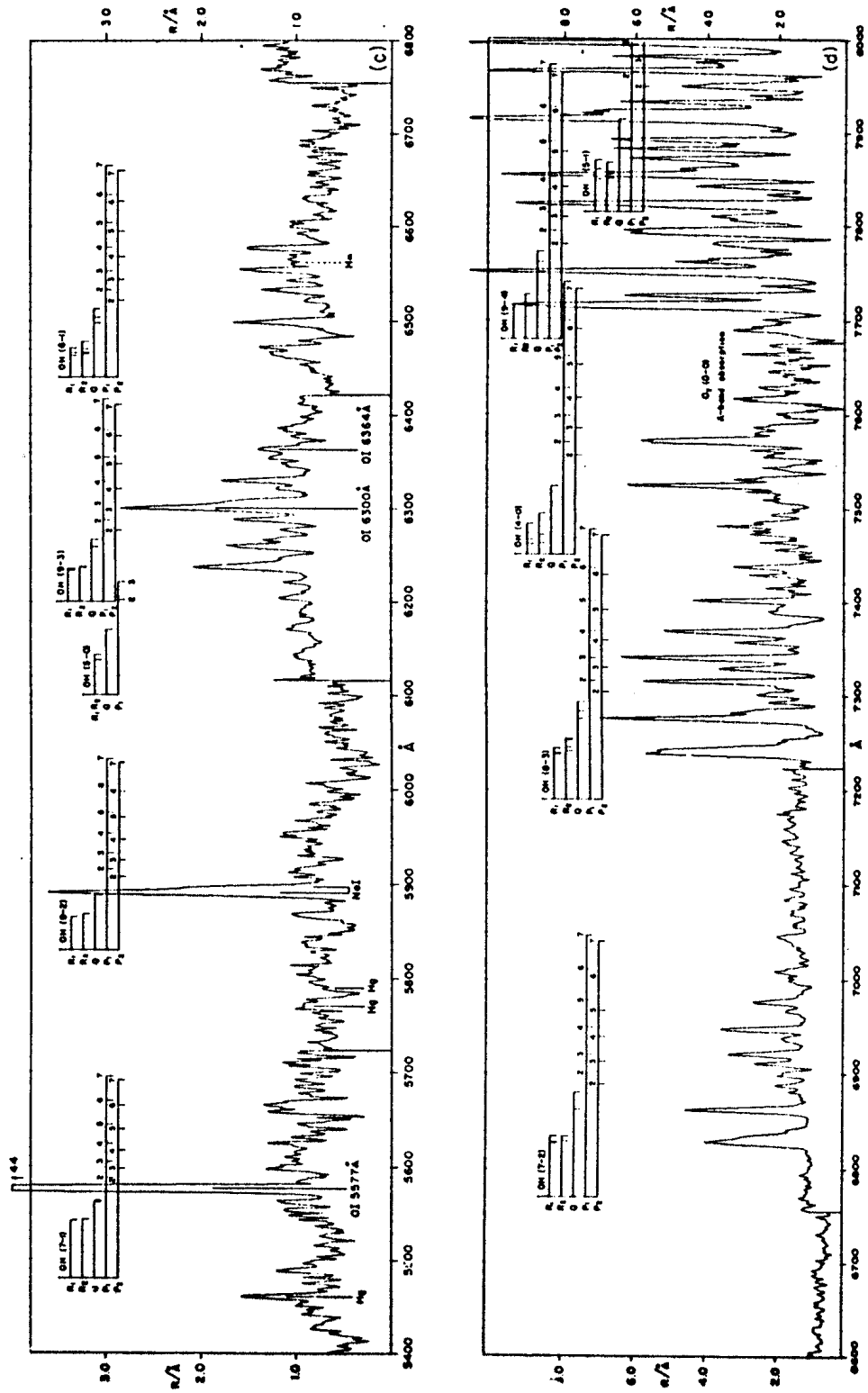
Figure 6.31– The Earth's airglow spectrum at night, showing the strong [O I] and Na I emission lines.
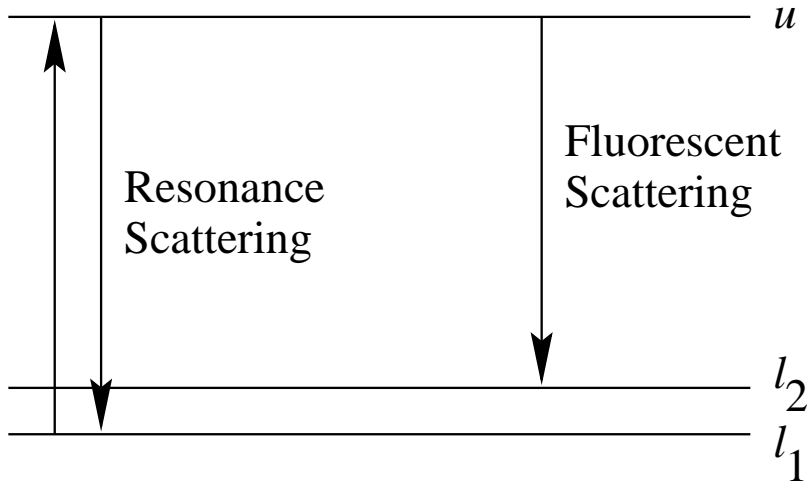
Figure 6.32– General energy level diagram for scattering processes.

Lyman-α emission has been found in the Earth's airglow, and arises from resonant scattering at very high altitudes. If this emission would be viewed from outside the atmosphere, it would look like a corona surrounding the Earth. The **Earth's corona** has been mapped from the Moon. Note that Ly α emission also arises from the hydrogen in the interplanetary medium, which comes from outer space. Analysis of the Ly α lines is complicated by the fact that the $^2S_{1/2} - {}^2P_{1/2}$ line is emitted isotropically, whereas the $^2S_{1/2} - {}^2P_{1/2}$ fine-structure component emits anisotropically. Another strong UV emission line in the upper atmosphere ($\sim$190 km) is the O I $2p^4\ {}^3P_{2,1,0} - 2p^33s\ {}^3S_1^\circ$ triplet at 1302, 1304, and 1306 Å. These lines are again produced by resonant scattering, and can be used as a probe of the O distribution in the high atmosphere.

The spectrographs on board the **A**tmospheric **E**xplorer satellites in the 1970's studied in detail a number of atomic and molecular lines arising in the thermosphere and ionosphere. The atoms of major interest in that study were $O^+({}^2P)$, $O({}^1D)$, $O({}^1S)$, $N({}^2D)$, and $Mg^+({}^2P_{1/2})$. The $O^+\ {}^2P \to {}^2D$ emission occurs at 7320 Å. Part of the population in the ^2P state may arise from ionization of O directly into the excited state. It can be shown that about 20% of the O^+ ions formed by either photoionization or by collisional ionization by photoelectrons are in the O^+ (^2P) state. The emission can be significantly quenched, even in the thermosphere up to 300 km altitude. Still, the amount of 7320 Å emission is a good measure of the ionization rate of oxygen.

Lines arising from the excited states of O and N again involve molecular processes and will therefore be discussed later. Note, however, that during the daytime at these altitudes, photoelectrons can excite some of the observed transitions as well.

The Mg^+ 3s $^2S_{1/2}$ – 3p $^2P_{1/2,3/2}$ doublet lines at ultraviolet wavelengths are again due to resonance fluorescence. These metallic ions are probably caused by ablations of meteoric matter near 100 km in the Earth's atmosphere. The species can then diffuse upward into the lower thermosphere, where charge exchange with positive ions will ionize Mg to form Mg^+. Mg^+ has a relatively long lifetime, in excess of one day, so that it is an excellent tracer of plasma motions in the ionosphere.
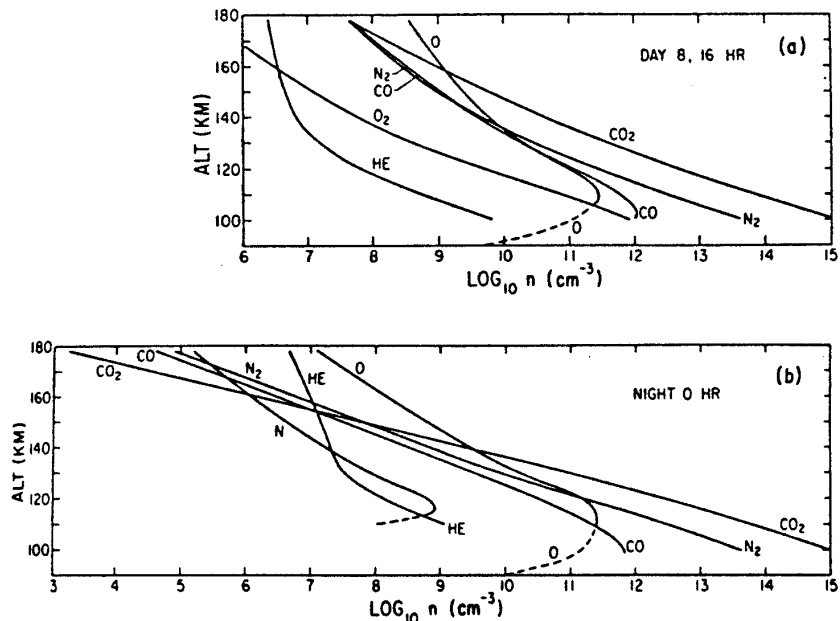
Figure 6.33–Densities for the Venus thermosphere on the day and night sides obtained from 1-D models based on Pioneer Venus and airglow data.
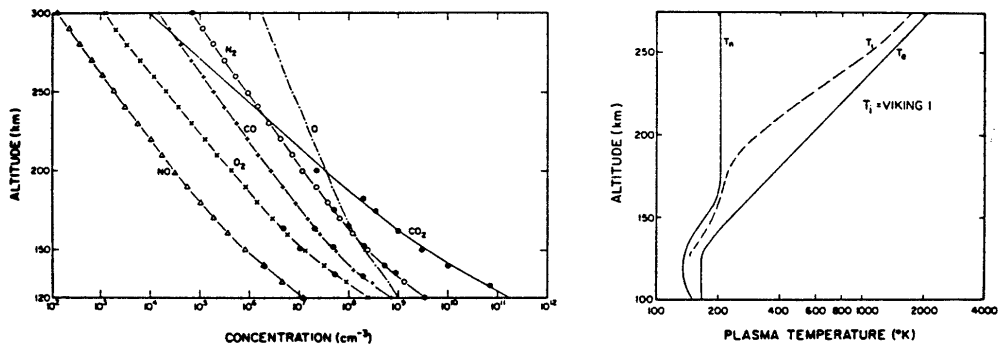

Figure 6.34– Model Martian thermosphere consistent with neutral and ion data from the two Viking landers. Neutral, ion, and electron temperatures are shown at the right.

6. Planetary Atmospheres

a) General Features

Many of the atoms and lines observed in the Earth's airglow are also seen in the atmospheres of the other planets, even though they differ considerably in composition from that of the Earth. Whereas the Earth's atmosphere consists mostly of N_2 (80%) and O_2 (20%), the atmospheres of Mars and Venus contain mostly CO_2 ($\sim$95%), with small amounts of N_2 and CO present. In contrast, Mercury has only a very tenuous atmosphere, whereas the outer planets Jupiter, Saturn, Uranus, and Neptune have very deep atmospheres of H_2 with small amounts of He and hydrocarbons such as methane along with ammonia and water. Figures 6.29-6.32 illustrate the temperature and density structure of the upper atmospheres of some of the planets.
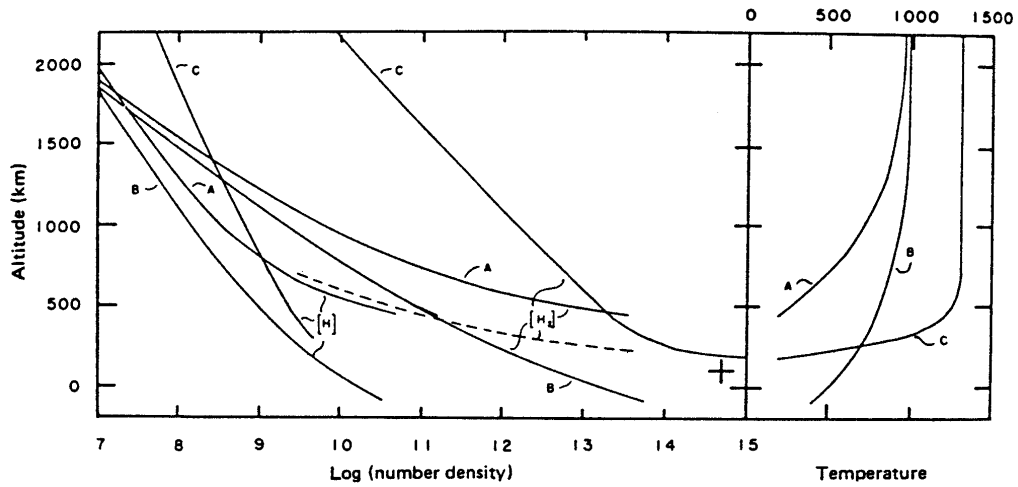
Figure 6.35– Jovian thermosphere, based on Voyager UV occultation data; the + point is from Earth-based stellar occultations. A and B are fits to the Voyager data, curve C fits ionospheric data with no other vertical transport than diffusion. He is omitted due to observational insensitivity.
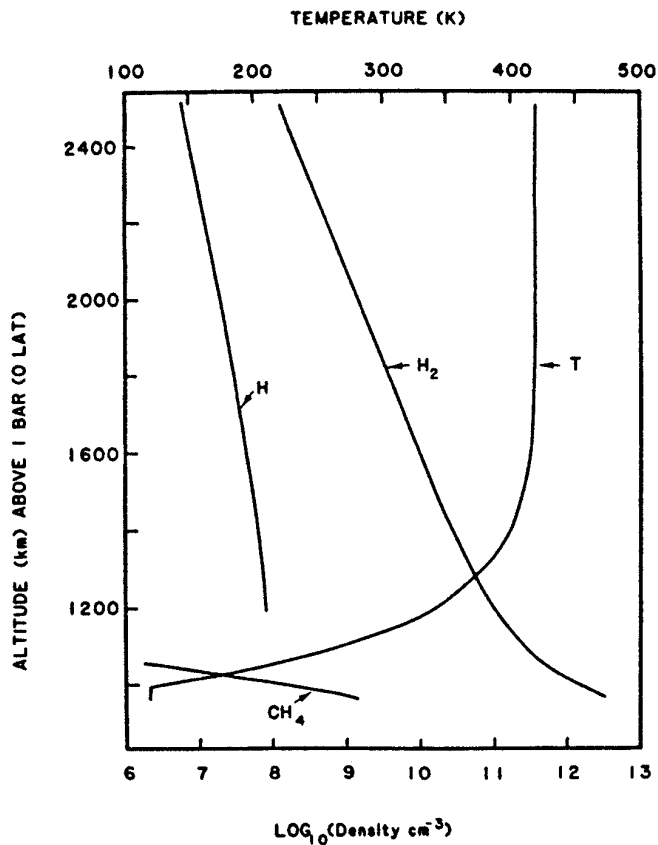

Figure 6.36– Saturn's thermosphere. As above, the occultation experiment was insensitive to He.

– 146 –

Planetary coronas arising from H Ly α emission due to resonant scattering have been observed on every planet from Mercury to Neptune, and even on Titan, the large satellite of Saturn. The He I $1s^2$ ^1S – $1s2p$ $^1P_1$ resonance line has also been seen on Jupiter, and can be used to determine the He abundance in the Jovian atmosphere, or, in the terminology of the planetary atmospheres, the $[He]/[H_2]$ *mixing ratio*.

Mercury has only a very tenuous atmosphere, but it does show, in addition to the H Ly α emission, the Na D emission lines due to resonant scattering by sunlight. Thus, Na must be an important constituent of Mercury.

In addition to the resonant $\lambda 1304$ Å triplet of O I, also the O I] $2p^4$ $^3P_{2,1}$ – $2p^3 3s$ $^5S^\circ_2$ lines at $\lambda 1356$ Å have been observed in the atmospheres of Mars and Venus. Because the ^3P – ^5S transition in forbidden within pure LS coupling, the oscillator strength for the $\lambda 1356$ Å transition is small, and the line cannot arise from resonance scattering. However, it can be produced by excitation by electron impact, so that the strength of the line is a measure of the amount of photoelectrons.

b) Nitrogen in Titan's Atmosphere

In the ultraviolet spectra of Titan obtained at the Voyager encounter, lines of molecular and atomic nitrogen can clearly be identified, as Figure 6.33 shows. Similar data are available for the Voyager Triton encounter. The principal lines observed are the N I 1134 Å $2p^3$ $^4S^\circ$ – $2s2p^4$ ^4P and 1200 Å $2p^2 3s$ $^4S^\circ$ – $2s2p^4 P$, and the N II 1085 Å $2p^2$ ^3P – $2s2p^3$ $^3D^\circ$ transitions. In addition, strong emission from the principal constituent, N_2, is seen in a series of Rydberg transitions (more later). The N emission arises primarily at altitudes between 3600 – 4000 km.
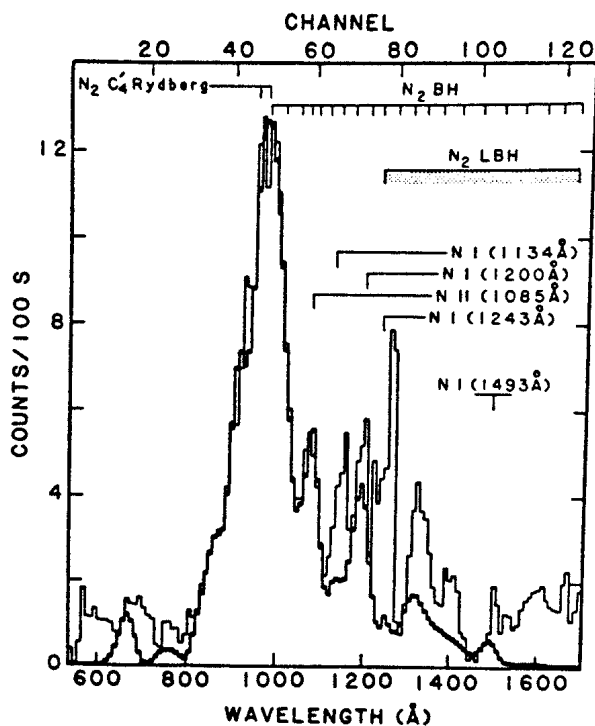

Figure 6.37– Ultraviolet spectrum of Titan's disk and a model fit involving the nitrogen lines and bands indicated.

Initially, it was suggested that the atomic lines result from collisional excitation by electrons from the magnetospheric plasma or by accelerated photoelectrons. Both the N I 1314 Å and 1200 Å lines, and the N II 1085 Å line, involve electric dipole allowed transitions, and should thus have comparable collisional excitation strengths. However, the N I 1134 Å line is much weaker than the N I 1200 Å and the N II 1085 Å lines. Thus, some other process must dominate the excitation, and the most likely one is electron impact dissociation of N_2:

$$N_2 \; + \; e^- \;\; \rightarrow \;\; e^- \; + \; N \; + \; N^+ \; + \; e^- \;\; , \qquad (6.49)$$

in which the products N and N^+ can be left in an excited electronic state, which subsequently decays through emission at 1200 and 1085 Å, respectively. The heavy line in Figure 6.33 is the corresponding model fit, which reproduces the spectral features of the nitrogen components quite well. The unidentified features in this spectrum probably belong to C I or C II. Energetic electrons with E>36 eV are required to produce the N II 1085 Å emission from N_2. An electron temperature of $T_e = 2 \times 10^5$ K has been used in the model fits, which is characteristic of auroral secondary electrons. This spectrum actually gave the first proof that N_2 is the principal gas on Titan (The same is true for Triton as well. Titan reference: Strobel and Shemansky 1982, *J. Geophys. Res.* **87**, 1361.).

c) Io's Plasma Torus

Io is the innermost of the Galilean satellites of Jupiter, at a distance of 5.9 R_J, where R_J is the radius of Jupiter. Its surface consists mostly of sulfur and SO_2 frost, although there is a somewhat controversial "detection" of CO_2 frost as well. At any one time, there are several volcanos or geysers erupting high into the atmosphere, ejecting large quantities of SO_2 vapor. Both ground based and Voyager I observations have shown that Io's orbit is surrounded by a torus containing atoms and ions of O, S, and some Na. The ionized part, or plasma, is at a high temperature, $T_e \sim 50,000$ K or 5 eV (1 eV = 11604.45 K), so that it radiates copiously in the ultraviolet region of the electromagnetic spectrum. Figure 6.34 shows the beautiful 2-D UV spectrum of the Jupiter system, and the lines of S III and O III are seen prominently. A good, short overview of the Io torus has been given by J.T. Trauger (1984, *Science* **226**, 337).

It is clear that Io must be the source of the material in the torus. However, the mechanisms for transferring material from Io are not yet fully understood. It most certainly involves sputtering of material from the surface of Io. In the process of sputtering, multiple collisions of atoms or molecules occur due to the impact of a fast ion, resulting in the ejection of one or more species in the backward direction. The torus arises because these ions can be trapped in Jupiter's magnetic field, and are thus forced to co-rotate with Jupiter at a speed of about 70 km/s. Io's orbital speed is only 17 km/s, so the ions overtake Io about twice a day, carrying a large amount of kinetic energy, $\sim$200-500 eV. Their thermal energy in the rotating coordinate frame is typically 1-10 eV. Figure 6.35 shows a sketch of the structure of the torus. Once can distinguish actually three different regions in the torus: A diffuse hot outer torus outside Io's orbit, the narrow ribbon-like hot inner torus closely confined to Io's orbit and seen in the S III and O III lines, and a relatively flat and isolated cool inner torus.
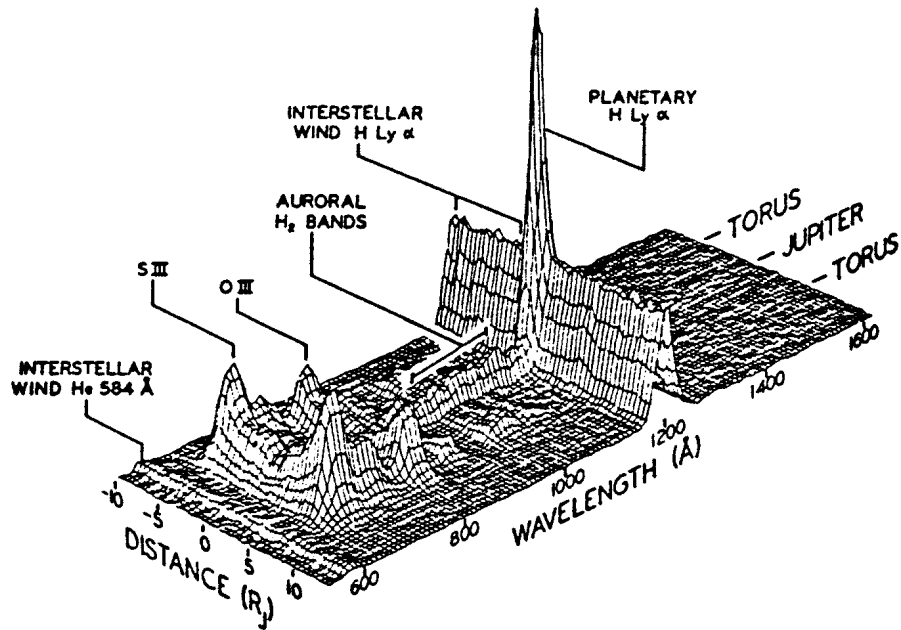
Figure 6.38–A panorama of UV spectra of the Jupiter system, viewed from a distance by Voyager 1. Light from Jupiter, the Io torus, and the interplanetary medium can all be seen [After Broadfoot *et al.* (1981)].
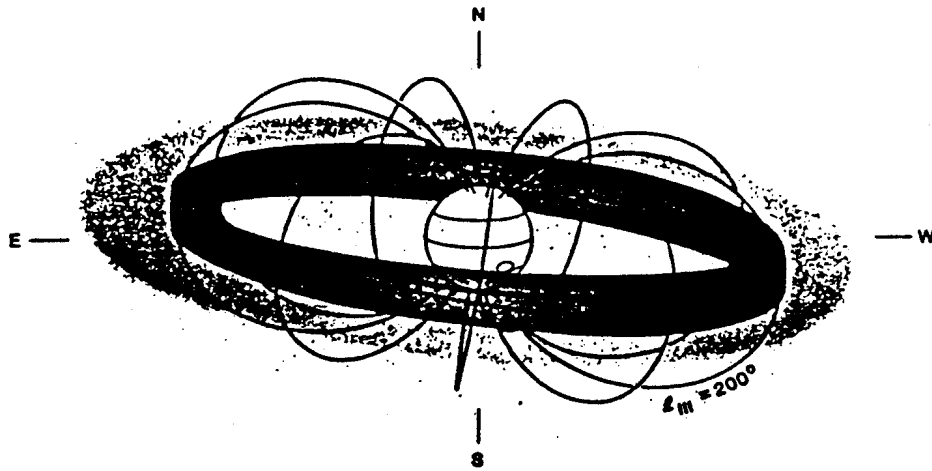

Figure 6.39– Sketch of the Jovian torus structure, with the three components discussed in the text illustrated. The torus structure is tilted 7° from the rotational equator, so that it appears at a variety of projected angles during each Jovian rotation.

Figure 6.36 shows the UV spectrum of the torus in more detail; visible and near-infrared emission lines have been detected as well. The data are entirely consistent with excitation by collisions with thermal electrons at an energy of about 5 eV. In fact, the spectrum is very similar to that of the ionized gas in planetary nebulae. It is the first astronomical nebula that can be studied by both classical astronomical techniques *and* by *in situ* measurements.

– 149 –

Just as for nebulae, the line ratios can be used to constrain the electron temperature and density. Remember that S III has the ground state configuration $3s^23p^2$, which gives rise, just as in the case of O III, to the terms ^3P, ^1D, and ^1S. The "auroral" line $^1S - {}^1D$ of [S III] occurs at 6312 Å, whereas the "nebular" line $^1D - {}^3P$ occurs at 9531 Å. Thus, these lines arise from levels with different excitation energies, so that their ratio should be temperature sensitive. The observed line ratio indicates a temperature T_e=50,000 K, or ~5 eV. The inner torus is found to be cooler, with an electron temperature of only 2 eV. The densities are found by considering the intensity ratio of the [S II] $^2D_{3/2,5/2} - {}^4S_{3/2}$ $\lambda6716/\lambda6731$ lines (see §VI.2a(v)). In the inner torus, n_{e-} is typically 3×10^3 cm^{-3}, and it is somewhat lower in the diffuse, hot torus and the inner torus (c.f. Figure 6.37). The strength of the lines is proportional to the product $n_{e-}n_{ion}$, so that once T_e and n_{e-} have been determined, the ion densities can be inferred as well.

Note that the radiative lifetimes of the upper levels of the ions ave very short, much shorter than the time it takes for the ion to diffuse outward. Thus, the excitation of a particular ion can indeed be considered in steady state. However, the recombination time and the ionization time are comparable to the diffusion loss times, so that the partitioning between SII, S III, S IV, etc. may not be in collisional equilibrium with the electron energy distribution. The deviations from this steady-state distribution can then be used as a measure of the diffusion loss rate.
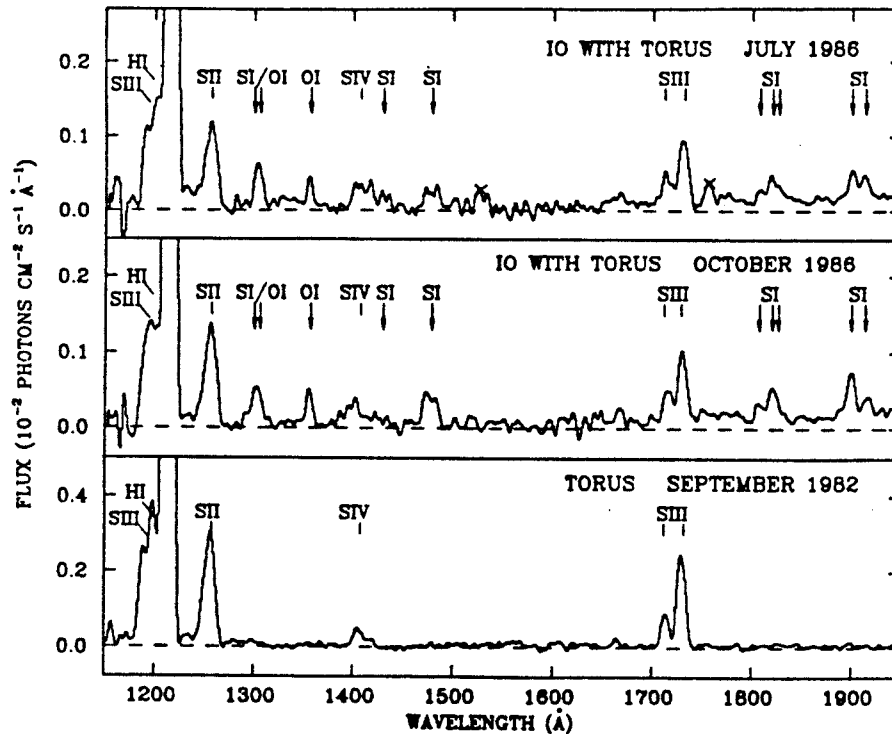

Figure 6.40– IUE spectra of Io and torus (top and center) from 1986 observations, together with a comparison torus spectrum (bottom) (IUE exposures SWP 28708, SWP 29430, and SWP 17829, respectively). The spectra are slightly smoothed. Arrows mark Io emission features, ticks mark torus emission features (and the geocoronal H I Ly α), and features marked with X are camera artifacts.

The initial Voyager data and ground-based spectra did not show any emission of O I, S I, or any ionized species, from Io itself; yet Io must be supplying fresh material to the torus. Very sensitive observations with the IUE satellite by Ballester *et al.* (1987, *Ap. J.* **319**, L33) have succeeded in detecting very weak lines of O I and S I, as Figure 6.36 shows (compare the top spectra with that at bottom). The emitting region is centered on Io and is less than five Io diameters across. The fact that some of the observed lines are intercombination lines (with small oscillator strengths) strongly suggests that electron impact, rather than resonant scattering, is the probable excitation mechanism. The ratio of the S I λ1429/λ1814 lines can be used to place limits on the electron temperature, and surprisingly, T_e <2 eV. This is significantly lower than the value of 5 eV found for the hot inner torus, so that the spectra are inconsistent with the simple picture that the emissions are produced by torus plasma impacting on an extended, low-density atmosphere of largely O and S. A significant part of these emissions must originate from the denser, collision dominated region of Io's atmosphere, probably by electron impact on SO_2.
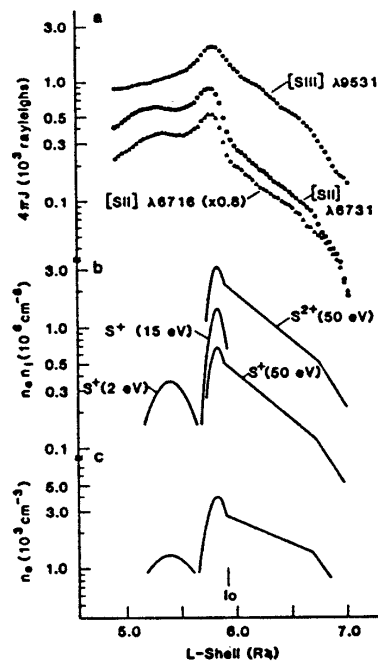

Figure 6.37– Representative comparison of data and models for a set of three images taken of the Jupiter system. (a) Curves showing a radial trace through the peak brightness positions. (b) Curves showing the radial structure at the centrifugal equator. The hot inner torus has been resolved into two components. (c) Curve showing the radial structure in apparent electron density at the equator.

References
Broadfoot *et al.* 1981, *J. Geophys. Res.* **86**, 8529.
Brown and Shemansky 1982, *Ap. J.* **263**, 433.
Moos *et al.* 1983, *Ap. J.* **275**, L19.
Moos *et al.* 1985, *Ap. J.* **294**, 369.
Trauger 1984, *Science* **226**, 337.
Ballester *et al.* 1987, *Ap. J.* **319**, L33